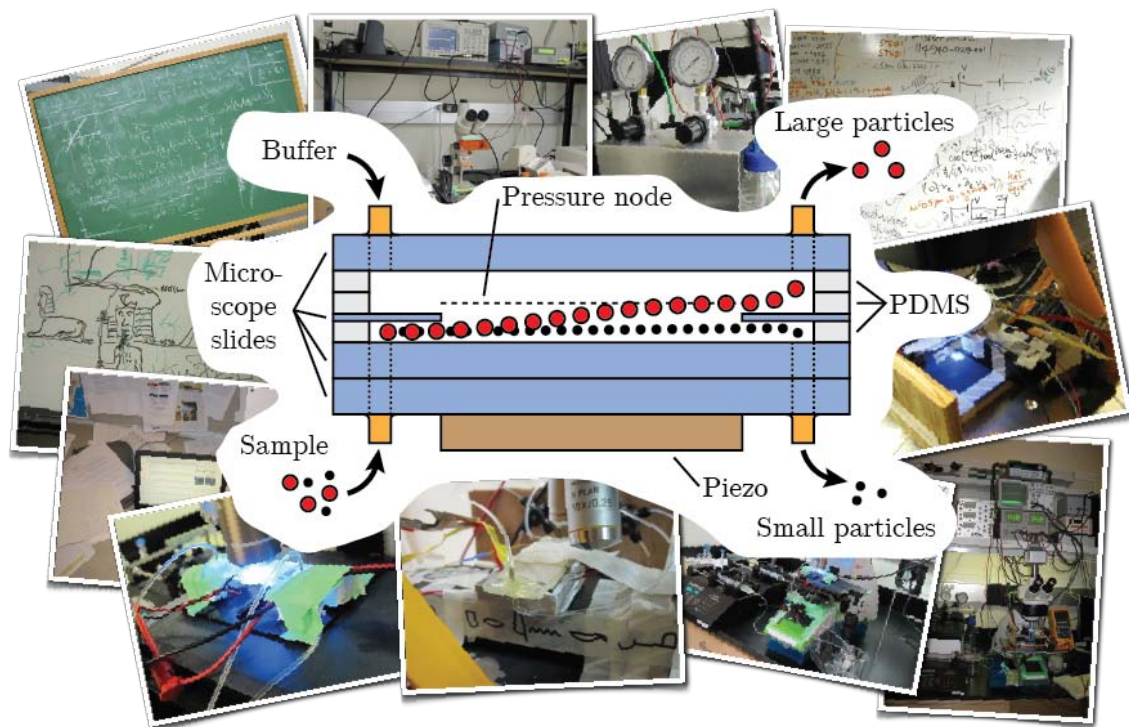


Bachelor Thesis, s094006

# Temperature-controlled, high-throughput acoustophoretic particle separation in microchannels

Christian Laut Ebbesen



Advisor: Henrik Bruus

Department of Micro- and Nanotechnology  
Technical University of Denmark

21 June 2010

**Front page illustration:** Schematic of the microfluidic device presented in this thesis overlaid on snapshots of some of the many steps involved in actually making such a novel design device functional: theory, numerical modeling, fabrication and many, many experimental trials and test probing the different physics of the device. The illustration shows the discrepancy between the seemingly extremely simple device design, and the amount of hard work that is needed to *actually* make the device work. It is inspired by the following comic by Jorge Cham of [www.phdcomics.com](http://www.phdcomics.com).

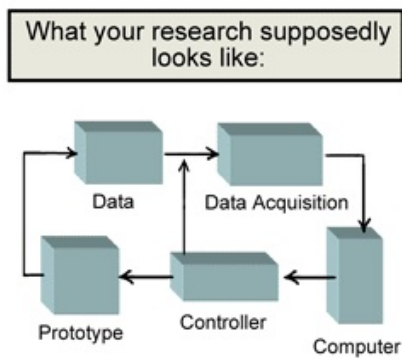


Figure 1. Experimental Diagram

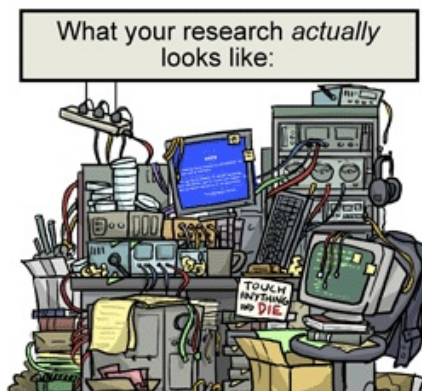


Figure 2. Experimental Mess

# Abstract

In this thesis we present a novel design for a microfluidic device capable of temperature-controlled, high-throughput acoustophoretic separation of microparticles. We introduce the necessary theory needed to perform a comprehensive analysis of the device design with special focus on the acoustic field, the flow patterns and the temperature field. We report having fabricated the device, optimized the device experimentally and achieved acoustophoretic microparticle-separation at 1 L/h flowrate, an improvement of 2 orders of magnitude over the state of the art. Using the theoretical concepts introduced, we explain the many intertwined physical considerations, that are prerequisites for our result. We introduce the importance of two concepts, previously not considered in the literature: temperature control and device geometry matching to the acoustic properties. Finally, we describe ongoing research on the device beyond this thesis.

*ABSTRACT*

# Resumé

I denne bacheloropgave præsenterer vi en hidtil uprøvet arkitektur for en mikrofluidt apparat til akustoforetisk separation af mikropartikler ved kontrolleret temperatur og høj gennemstrømning. Vi introducerer den teori, som er nødvendigt for at lave en fyldestgørende analyse af apparatet med speciel fokus på det akustiske felt, strømningsmønstret og temperaturfeltet. Vi beretter at have bygget apparatet, optimeret det eksperimentelt og opnået akustoforetisk separation af mikropartikler ved en gennemstrømning på 1 liter pr. time, hvilket er en forbedring på 2 størrelsesordner i forhold til hidtil opnået gennemstrømning i lignende apparater. Ved hjælp af den indførte teori, gennemgår vi de mange sammenspillende fysiske overvejelser, som er forudsætningen for vores resultat. Vi gør opmærksom på vigtigheden af to ting, som ikke er blevet beskrevet i litteraturen før: temperaturkontrol og tilpasning af apparatets arkitektur til de akustiske egenskaber. Slutteligt beskriver vi aktiv forskning på apparatet som fortsætter efter afleveringen af denne opgave.

*RESUME*

# Preface

This thesis is submitted in order to fulfill the requirements to obtain the degree of Bachelor of Science in Biophysics at the Niels Bohr Institute, University of Copenhagen. The research presented corresponds to a credit of 15 ECTS points and formally the thesis is written as an external thesis at the Technical University of Denmark which will award the ECTS points.

The research was carried out from February 2010 to June 2010 under supervision by Prof. Henrik Bruus, head of the Theoretical Microfluidics Group (TMF) at the Department of Micro- and Nanotechnology at the Technical University of Denmark, while he was on sabbatical visiting the the Soh Lab in the Department of Mechanical Engineering at University of California, Santa Barbara. The project was done in collaboration with Dr. Jonathan D. Adams of the Soh Lab.

I would like to thank Prof. Henrik Bruus for being a fantastic advisor throughout the project. His enthusiastic advise on all things, mostly physics, and his experienced physical intuition has been extremely inspiring. I am deeply grateful to Prof. Henrik Bruus for agreeing to supervise my work, for giving me this amazing opportunity to do research and make academic contacts and friends at one of the world's top universities<sup>1</sup> and for bringing me along to seminars at University of California, Riverside and University of Southern California.

I would like to thank Dr. Jonathan D. Adams for a wonderful collaboration. His helpfulness and patience is endless and I have learned a lot from working with him in the lab. I look very much forward to taking our work to the next level: Liters-per-hour flowrates of whole human blood. It will be so much fun!

Furthermore, I would like to thank Prof. H. Tom Soh of the Department of Mechanical Engineering and Department of Materials, University of California, Santa Barbara for his academic advise and support throughout the project.

I would also like to thank the rest of the Santa Barbara TMF group contingent, Rune Barnkob, Mathias Bækbo Andersen, Kasper Kristensen and Mikkel Settnes, and our man in Paris, sorry, Stanford, Søren Vedel, for a fantastic working (and also not-working) atmosphere and many fruitful discussions. And special thanks to my two fellow B.Sc. students Jesper Toft Kristensen and Kristian Lund Jensen for keeping the Cali mentali anytime, anywhere from deserted late-night labs to crowded coffeshops.

In addition, I would also like to thank my office mates Kuangwen Hsieh and his turtles

---

<sup>1</sup>At the Leiden Ranking 2008 with *size-independent, field-normalized average impact 'crown indicator'* CPP/FCSm UC Santa Barbara engineering department is ranked 6th in the world.

## PREFACE

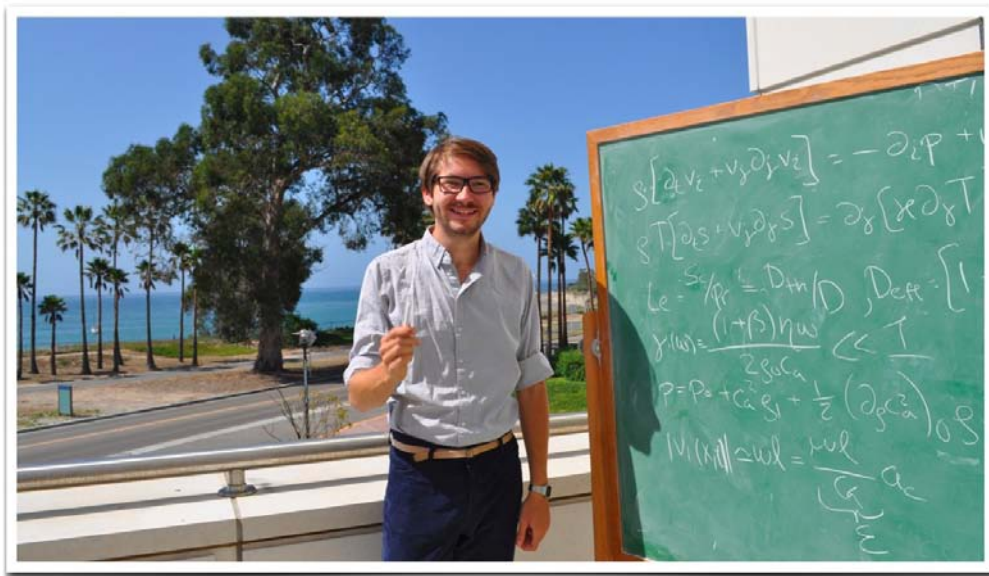
as well as the rest of the Soh Lab, especially Scott Ferguson, Jinpeng Wang and Lore Dobler, for welcoming me into the lab.

Moreover, I would like extend my humble thanks to Frank Sinatra, Humphrey Bogart, Billie Holiday and the city of Los Angeles for playing vital roles at critical stages of the project.

Finally, I would like to thank all my friends and family for skype, email and facebook advice on everything, mostly not physics, during my stay in California with special thanks to my sister, mother and father.



Christian Laut Ebbesen  
University of California, Santa Barbara  
20 June 2010



# Contents

List of figures

List of tables

List of symbols

<b>1</b>	<b>Introduction</b>	<b>1</b>
<b>2</b>	<b>Theory and governing equations</b>	<b>3</b>
2.1	Governing equations of microfluidic flow . . . . .	3
2.1.1	Incompressible flow in microchannels . . . . .	4
2.1.2	Poiseuille flow . . . . .	4
2.1.3	Diffusion phenomena . . . . .	5
2.1.4	Heat transfer . . . . .	6
2.1.5	Dimensionless numbers . . . . .	6
2.1.6	Equivalent circuit theory . . . . .	9
2.2	Introduction to acoustophoretic separation . . . . .	9
2.2.1	The acoustic wave equations in microfluidics . . . . .	10
2.2.2	Setting up acoustic resonances . . . . .	12
2.2.3	Modelling resonances in actual microchips . . . . .	13
2.2.4	Second order effects: Acoustic forces . . . . .	14
2.2.5	Acoustophoresis in resonant microchannels . . . . .	16
2.3	Introduction to finite element method solutions. . . . .	19
<b>3</b>	<b>High-throughput device</b>	<b>21</b>
3.1	Introduction to high-throughput design . . . . .	21
3.2	Device fabrication . . . . .	22
3.2.1	Preparation . . . . .	22
3.2.2	Assembly . . . . .	24
3.2.3	External setup . . . . .	27
3.3	Theoretical estimate of resonant frequency . . . . .	28
3.3.1	Validity of 1D-model . . . . .	28
3.3.2	Calculation of resonant frequency . . . . .	28
3.4	Device plumbing . . . . .	31

*CONTENTS*

3.4.1	Flow and shear stress . . . . .	31
3.4.2	External tubing . . . . .	34
3.5	Main separation results . . . . .	35
3.6	Frequency modulation. . . . .	40
3.7	Temperature effects . . . . .	42
<b>4</b>	<b>Conclusion and future work</b>	<b>45</b>
<b>A</b>	<b>Abstract for micro-TAS 2010</b>	<b>49</b>

# List of Figures

2.1	Flow in rectangular microchannel. . . . .	4
2.2	Taylor–Aris dispersion. . . . .	8
2.3	The acoustic radiation force in a resonant microchannel . . . . .	17
2.4	Acoustophoresis . . . . .	18
2.5	Finite element solutions . . . . .	19
3.1	Device design schematic and temperature controlled device setup. . . . .	23
3.2	Usual acoustophoresis design vs. high-throughput design. . . . .	24
3.3	Device layers and cross-sectional views. . . . .	25
3.4	Device assembly and assembled devices . . . . .	26
3.5	Second-generation design of outlets . . . . .	27
3.6	Validity of 1D resonance calculation . . . . .	29
3.7	1D approximation of device geometry . . . . .	31
3.8	Theoretical calculations of resonance frequencies . . . . .	32
3.9	Finite element method calculation of flow in device . . . . .	33
3.10	Device plumbing . . . . .	36
3.11	Calculation of device resistance using equivalent circuit theory . . . . .	37
3.12	Experimental determination of outlet flow ratio . . . . .	38
3.13	Experimental separation results . . . . .	39
3.14	Experimentally observed temperature effects . . . . .	41
3.15	Finite element method calculation of device temperature field. . . . .	43

*LIST OF FIGURES*

# List of Tables

2.1	Typical parameters for ultrasound waves in water-filled microchannels. . . .	11
2.2	Acoustic properties of typical Lab-on-a-chip materials. . . . .	14
3.1	Thermal properties of water and pyrex glass . . . . .	44

*LIST OF TABLES*

# List of symbols

Symbol	Description	Unit
$\mathcal{A}$	An area	$\text{m}^2$
$a$	A small particle radius	$\text{m}$
$c_a$	Speed of sound	$\text{m/s}$
$c_\alpha$	Concentration of solute $\alpha$	$\text{m}^{-3}$
$c_p$	Heat capacity at constant pressure	$\text{J}/(\text{kg K})$
$D$	Diffusion constant	$\text{m}^2/\text{s}$
$E$	Energy	$\text{J}$
$\eta$	Dynamic viscosity	$\text{Pa s}$
$\dot{\gamma}$	Shear rate	$\text{s}^{-1}$
$\mathbf{F}$	Force vector	$\text{N}$
$\mathbf{f}$	Force density vector	$\text{N}/\text{m}^3$
$f$	Frequency	$\text{Hz}$
$h$	Height	$\text{m}$
$\mathbf{J}_A$	Flux vector for some quantity A	$[A]/(\text{m}^2 \text{s})$
$\mathbf{k}$	Wave vector	$\text{m}^{-1}$
$\kappa$	Thermal conductivity	$\text{W}/(\text{m K})$
$L$	Length	$\text{m}$
$l$	Wave number in width dimension	
$\ell$	A small length	$\text{m}$
$\lambda$	Wavelength	$\text{m}$
$m$	Wave number in length dimension	
$\mathbf{n}$	Surface normal vector	
$n$	Wave number in height dimension	
$\omega$	Angular frequency	$\text{s}^{-1}$
$\mathbf{P}$	Momentum vector	$(\text{kg m})/\text{s}$
$p$	Pressure	$\text{Pa}$
$\Phi$	Acoustophoretic contrast factor	
$\phi$	Velocity potential	$\text{m}^2/\text{s}$
$Q$	Volumetric flowrate	$\text{m}^3/\text{s}$
$R_{\text{hyd}}$	Hydraulic resistance	$\text{Pa s}/\text{m}^3$
$\mathbf{r}$	Position vector	$\text{m}$
$\rho$	Mass density	$\text{kg}/\text{m}^3$

*LIST OF SYMBOLS*

Symbol	Description	Unit
$s$	Entropy pr. unit mass	J/(K m <sup>3</sup> )
$\sigma$	Stress tensor	N/m <sup>2</sup>
$T$	Temperature	K
$t$	Particle transfer rate	
$\tau$	Shear stress	Pa
$U$	Potential	J
$V$	Voltage	V
$\mathcal{V}$	A volume	m <sup>3</sup>
$\mathbf{v}$	Velocity vector	m/s
$w$	Width	m
$x$	Position coordinate	m
$y$	Position coordinate	m
$z$	Position coordinate	m

# Chapter 1

## Introduction

During recent years several groups have demonstrated the use of acoustic forces in microsystems for gentle, label-free cell- and particle separation[27, 1, 16, 19, 10, 23, 14]. This technique has been dubbed *acoustophoresis* and has a wide range of valuable applications in medical diagnostics, cell-based biotechnology and biomedical engineering, where there is a need for particle separation systems capable of separations at high purity and throughput, beyond what is presently offered by traditional methods e.g. fluorescence activated cell sorting and centrifugation. The wide-ranging applications of the technique presented in the literature includes an acoustic whole blood plasmapheresis chip for prostate specific antigen microarray diagnostics[15], acoustic differential extraction for forensic analysis of sexual assault evidence[20], acoustophoretic synchronization of mammalian cells[27] and precondition in protein and lipid content quality control of raw milk samples[9].

One important shortcoming of previously reported microfluidic systems has been the inherently low throughput of microchannel devices. In this thesis, we present a microfluidic device capable of very high-throughput ( $> 1$  L/h) acoustophoretic particle-separation, an improvement of 2 orders of magnitude over previous work in the field[8, 16]. Furthermore, our device is constructed from low-cost materials using rapid-prototyping techniques which pave the way for easy utilization of high-throughput acoustophoretic particle/cell separation in other labs.

We use a combination of thorough theoretical analysis of the device physics and experimental investigations to draw attention to especially two points that have not been considered in the field before: (*i*) The importance of controlling the device temperature and (*ii*) the importance of designing the device geometry to support strong acoustic fields.

The work done in the thesis is new research, which we intend to publish in the scientific literature. Before the deadline of this thesis, we have already submitted an abstract to The 14th International Conference on Miniaturized Systems for Chemistry and Life Sciences (micro-TAS or  $\mu$ TAS), to be held 3 - 7 October 2010 in Groningen, The Netherlands. This abstract is reprinted in Appendix A of this thesis. The casual, curious reader is advised to look this abstract over for a quick summary of the work done in this thesis.

The thesis itself is structured in two parts; In the first part of the thesis, we introduce the basic physical principles necessary to understand the workings of acoustophoretic

particle separation. In the second half of the thesis, we present our new device and apply the theoretical concepts introduced in first part of the thesis to analyse the device with special focus on the acoustic, mechanical and thermal properties to describe the acoustic forces, the microfluidic flow and temperature effects. The acoustic, mechanical and thermal properties of the device are very much intertwined and a good understanding of all the physics simultaneously has allowed us to optimize our good device design. In this thesis we attempt our best to present the analysis as a cohesive story with a logical progression.

Finally, we briefly discuss actual biological applications and further optimization of the device which are part of ongoing work on the device beyond this thesis.

## Chapter 2

# Theory and governing equations

We shall begin this thesis by introducing the governing equations for the relevant physical fields, so that all theory and notation is familiar to the reader in the subsequent chapters. This short review of theory is based on the excellent reviews by Bruus [5, 6] and Landau & Lifshitz [12, 13]. We use the Einstein notation for shorthand notation of vectors, sums and derivatives.

### 2.1 Governing equations of microfluidic flow

The governing equations for the hydrodynamics of microfluidics can be derived by considering conservation of mass, momentum and energy in the continuum mechanics description. In the general case, the conservation of momentum for a fluid can be written as,

$$\rho[\partial_t v_i + v_j \partial_j v_i] = \partial_j \sigma_{ij} + f_i, \quad (2.1)$$

where  $v_i$  is the velocity,  $\rho$  is the density,  $\sigma_{ij}$  is the full stress tensor and  $f_i$  is the sum of body force densities acting on the fluid. In the case of a compressible Newtonian fluid in the absence of body forces, this reduces to the famous Navier–Stokes equation,

$$\rho[\partial_t v_i + v_j \partial_j v_i] = -\partial_i p + \eta \partial_j^2 v_i + \beta \eta \partial_i (\partial_j v_j), \quad (2.2)$$

where  $p$  is the pressure,  $\eta$  is the bulk dynamic viscosity and  $\beta \equiv \zeta/\eta + 1/3 \approx 5/3$  is the dimensionless ratio between the bulk dynamic viscosity,  $\eta$ , and the second compressional viscosity,  $\zeta$ . Conservation of mass leads to the continuity equation,

$$\partial_t \rho = -\partial_j (\rho v_j), \quad (2.3)$$

stating that temporal density change in a domain must be due to a non-zero mass flux at the domain boundary. Besides these equations, we will often also make use of different thermodynamic relations to write down equations of state, i.e.  $p = p(\rho)$ , depending on the problem, we want to analyze.

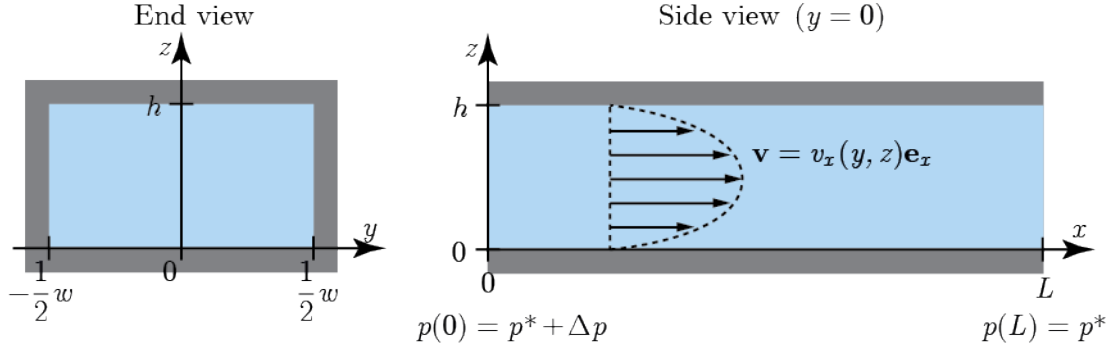


Figure 2.1: (a) End view of a water-filled section of a rectangular microfluidic channel of width  $w$  and height  $h$ . (b) Side view at  $y = 0$  of a water-filled section of a rectangular microfluidic channel of length  $L$  and height  $h$  with an applied overpressure  $\Delta p$  at  $x = 0$  showing approximately parabolic velocity profile from Eq. (2.9) (dashed black lines and black vector arrows) in the limit where  $h \ll w$ .

### 2.1.1 Incompressible flow in microchannels

In microfluidics, central to this work, where the flow velocities are much less than the velocity of pressure waves (speed of sound) in water,  $c_a = 1482$  m/s, we can treat the fluid as incompressible. This means, that  $\rho$  is a constant in space and time, and the continuity equation, Eq. (2.3), reduces to

$$\partial_i v_i = 0, \quad (2.4)$$

and Eq. (2.2) simplifies to the incompressible Navier–Stokes equation,

$$\rho[\partial_t v_i + v_j \partial_j v_i] = -\partial_i p + \eta \partial_j^2 v_i. \quad (2.5)$$

### 2.1.2 Poiseuille flow

We will need to describe pressure-driven Poiseuille flow<sup>1</sup> in a microchannel with a rectangular cross section. Consider a section of of a microchannel of width  $w$ , height  $h$  and length  $L$  as shown in Fig. 2.1. By applying an overpressure  $\Delta p$  over some hydrostatic pressure  $p^*$  to one end of the channel, we can drive a flow. From symmetry considerations we see that the velocity field only has an  $x$ -component and will depend only on  $y$  and  $z$ ,

$$\mathbf{v}(x, y, z) = v_x(y, z)\mathbf{e}_x, \quad (2.6)$$

and due to translational invariance along the channel, we have  $\partial_x p = -\Delta p/L$ . By inserting this into the incompressible Navier–Stokes equation, and demanding a steady state solution ( $\partial_t v_i = 0$ ), we are left with

$$[\partial_y^2 + \partial_z^2] v_x(y, z) = -\frac{\Delta p}{\eta L} \quad \text{for} \quad -\frac{1}{2}w < y < \frac{1}{2}w, \quad 0 < z < h. \quad (2.7)$$

<sup>1</sup>Pressure driven flow is called Poiseuille flow after Jean Louis Marie Poiseuille (1797-1869) who studied this phenomenon in relation to human blood flow in small tubes in his 1828 dissertation entitled *Recherches sur la force du coeur aortique*[24].

and we have the no-slip boundary condition, that the velocity must go to zero at the channel wall,

$$v_x(\pm \frac{1}{2}w, z) = 0 \quad v_x(y, 0) = 0 \quad v_x(y, h) = 0 \quad (2.8)$$

Using a Fourier series expansion, it is straightforward albeit laborious to show that the velocity field takes the shape

$$v_x(y, z) = \frac{4h^2}{\pi^3 \eta L} \sum_{n, \text{odd}}^{\infty} \frac{1}{n^3} \left[ 1 - \frac{\cosh(n\pi \frac{y}{h})}{\cosh(n\pi \frac{w}{2h})} \right] \sin\left(n\pi \frac{z}{h}\right). \quad (2.9)$$

In the limit of a very flat and very wide channel ( $h/w \rightarrow 0$ ), this velocity profile resembles the simple parabolic velocity profile known from flow between two infinite parallel plates, see Fig. 2.1, and we can approximate the total volumetric flowrate,  $Q$ , of the channel as

$$Q = 2 \int_0^{\frac{1}{2}w} dy \int_0^h dz v_x(y, z) \approx \frac{h^3 w \Delta p}{12 \eta L} \left[ 1 - 0.630 \frac{h}{w} \right], \quad \text{for } h \ll w. \quad (2.10)$$

### 2.1.3 Diffusion phenomena

Diffusion is the spontaneous motion of particles (the solute) in a liquid medium (the solvent) to even out concentration inhomogeneities. Conceptually, it can be thought of as arising from random motion of the particles due to fluctuations in thermal energy (or as an entropy driven process, cf. the second law of thermodynamics). The random motion of particles will eventually distribute the solute evenly in the solvent. To first order, we can describe the diffusion-driven flux of particles,  $J_i$ , by Fick's law,

$$J_i = -D_\alpha \partial_i c_\alpha, \quad (2.11)$$

where  $c_\alpha(\mathbf{r}, t)$  is the concentration field of some solute  $\alpha$  and  $D_\alpha$  is the diffusion constant. By considering Fick's law and balancing the gradient of the chemical potential of the solution with the Stokes drag force,  $F_i = -6\pi\eta a v_i$ , where  $a$  is the effective radius of the solute, we can derive the Einstein relation for the diffusion constant,

$$D_\alpha = \frac{k_B T}{6\pi\eta a}. \quad (2.12)$$

For a typical 3  $\mu\text{m}$  microparticle in water at 300 K, we find  $D_\alpha = 1.5 \times 10^{-13} \text{ m}^2\text{s}^{-1}$ . Assuming no solute concentration sources or sinks (i.e. chemical reactions for a species of molecules), we can write the conservation of solute as the so-called convection-diffusion equation,

$$\partial_t c_\alpha + v_j \partial_j c_\alpha = D_\alpha \partial_j^2 c_\alpha, \quad (2.13)$$

stating that the temporal change of concentration of the solute  $\alpha$  in some domain is only due to advection or a non-zero diffusion driven solute flux at the domain boundary. In a fluid at rest with no velocity field, Eq. (2.13) becomes the diffusion equation,

$$\partial_t c_\alpha = D_\alpha \partial_j^2 c_\alpha, \quad (2.14)$$

From simple dimensional analysis of this equation, we can arrive at the useful relation,

$$L_0^2 = D_\alpha T_0, \quad (2.15)$$

where  $L_0$  and  $T_0$  is a characteristic length and time over which the concentration  $c_\alpha(\mathbf{r}, t)$  varies.

#### 2.1.4 Heat transfer

Similar to the conservation of momentum and solute, we can also write down an equation for the conservation of energy. In the general case disregarding energy sources or sinks, a temporal change of energy is only due to energy convection, work by stress forces and thermal conduction. From this, we can derive the heat equation,

$$\rho T [\partial_t s + v_j \partial_j s] = \partial_j [\kappa \partial_j T] + \sigma'_{jk} \partial_k v_j, \quad (2.16)$$

where  $T$  is the temperature,  $\kappa$  is the thermal conductivity,  $s$  is the entropy pr. unit mass and  $\sigma'_{jk}$  is the viscous stress tensor. By employing the well-known thermodynamic relation, that  $s = s(T, p)$  and assuming constant pressure ( $v_i \ll c_a$ ), we can rewrite the derivatives  $\partial_t s = (\partial_T s)_p \partial_t T$  and  $\partial_i s = (\partial_T s)_p \partial_i T$  and introduce the heat capacity at constant pressure  $c_p = T(\partial_T s)_p$ . In microfluidics, we can often neglect the temperature dependence of  $\rho$ ,  $\eta$ ,  $\kappa$  and  $c_p$  and then Eq. (2.16) reduces to

$$\partial_t T + v_j \partial_j T = D_{\text{th}} \partial_j^2 T + \frac{\eta}{2\rho c_p} (\partial_k v_i + \partial_i v_k)^2, \quad (2.17)$$

where we have explicitly written out the cross-term from the viscous stress tensor and introduced the thermal diffusion constant,

$$D_{\text{th}} \equiv \frac{\kappa}{\rho c_p}. \quad (2.18)$$

The thermal diffusion constant of water at 20 °C is  $D_{\text{th}} = 1.43 \times 10^{-7} \text{ m}^2\text{s}^{-1}$  and it is a relevant quantity for studying heat transfer in a fluid at rest, where Eq. (2.17) reduces to a simple diffusion equation, known as Fourier's equation,

$$\partial_t T = D_{\text{th}} \partial_j^2 T. \quad (2.19)$$

Once again, we can use dimensional analysis to arrive at a useful relation between a characteristic length and time in thermal diffusion,

$$L_0^2 = D_{\text{th}} T_0. \quad (2.20)$$

#### 2.1.5 Dimensionless numbers

In the subsequent treatment of our microfluidic device, it is convenient to define some dimensionless numbers relating the magnitude of physical phenomena. These dimensionless numbers provide an easy way of assessing which physical phenomenon is dominant in varying physical situations.

We can make the incompressible Navier-Stokes equation, Eq. (2.5), dimensionless by scaling the variables to a characteristic length,  $L_0$ , velocity,  $V_0$ , time,  $T_0 = L_0/V_0$ , and pressure,  $P_0 = \eta V_0/L_0$ , and scaling the derivatives as  $\partial_t = (1/T_0)\tilde{\partial}_t$  and  $\partial_i = (1/L_0)\tilde{\partial}_i$ . The dimensionless equation then reads

$$Re \left[ \tilde{\partial}_t \tilde{v}_i + \tilde{v}_j \tilde{\partial}_j \tilde{v}_i \right] = -\tilde{\partial}_i \tilde{p} + \tilde{\partial}_j^2 \tilde{v}_i, \quad (2.21)$$

where  $\tilde{p} = p/P_0$  and  $\tilde{v} = v_i/V_0$  are dimensionless variables. Here we have introduced the dimensionless Reynolds number,

$$Re \equiv \frac{\rho V_0 L_0}{\eta}. \quad (2.22)$$

From Eq. (2.21) we see, that the viscous term,  $\tilde{\partial}_j^2 \tilde{v}_i$ , dominates if  $Re \ll 1$ , whereas if the inertial term,  $\tilde{v}_j \tilde{\partial}_j \tilde{v}_i$ , dominates  $Re \gg 1$ . Thusly, computing the Reynolds number for a given flow is a way to asses whether the flow is dominated by inertial forces or viscous forces. If we let  $Re \ll 1$  and return to physical values, Eq. (2.21) approximates to the Stokes equation,

$$0 = -\partial_i p + \eta \partial_j^2 v_i, \quad (2.23)$$

and from this it is evident, that if  $Re \ll 1$  the flow can only be laminar. This is typically the case in microfluidics.

Using the same approach, we can also make the advection-diffusion equation, Eq. (2.13) dimensionless. For simplicity, we choose advection and diffusion in a circular tube of radius  $R$ . Defining  $x$  along the channel length and  $r$  and the radial coordinate, see Fig. 2.2, we can introduce a characteristic length  $L_0$  and velocity  $V_0$  and write

$$Pé \partial_{\tilde{t}} c_\alpha + Pé \frac{R}{L_0} \tilde{v}_x \partial_{\tilde{x}} c_\alpha = \left( \partial_{\tilde{r}}^2 c_\alpha + \frac{1}{\tilde{r}} \partial_{\tilde{r}} c_\alpha \right) + \frac{R^2}{L_0^2} \partial_{\tilde{x}}^2 c_\alpha \quad (2.24)$$

where  $\tilde{r} = r/R$ ,  $\tilde{v}_x = v_x/V_0$  and  $\tilde{x} = x/L_0$  are dimensionless coordinates and we have kept the concentration,  $c_\alpha$ , unchanged. Here, we have introduced the so-called Péclet number,

$$Pé \equiv \frac{V_0 R}{D_\alpha}. \quad (2.25)$$

We see, that for high Péclet numbers the left hand side of the equation dominates and the solute is primarily spread by advection. For low Péclet numbers, the right hand side of the equation dominates and the solute is primarily spread by diffusion.

In the general case it turns out that the Péclet number will always depend on some characteristic length  $L_0$  and from dimensional analysis, we see that the Péclet number can be thought of as the ratio between a characteristic diffusion time and a characteristic advection time,

$$Pé \equiv \frac{\text{diffusion time}}{\text{advection time}} = \frac{V_0 L_0}{D_\alpha}. \quad (2.26)$$

It is worth to note, that in Eq. (2.24), we see that there is a factor of  $R^2/L_0^2$  scaling between the radial diffusion and the axial diffusion on the right hand side of the equation.



This is also a general feature and gives rise to the so-called Taylor-Aris dispersion leading to an increased effective diffusion constant for the solute. In the regime, where  $Pé \gg 1$ , we have,

$$D_{\text{eff}} = \left[ 1 + \frac{1}{48} P\acute{e}^2 \right] D, \quad (2.27)$$

Utilizing the similarity between solute diffusion and thermal diffusion, we can also introduce a thermal Péclet number, expressing the ratio between the effect of thermal diffusion and thermal advection,

$$P\acute{e}_{\text{th}} \equiv \frac{\text{thermal diffusion time}}{\text{thermal advection time}} = \frac{V_0 L_0}{D_{\text{th}}}, \quad (2.28)$$

where  $L_0$  and  $V_0$  is a characteristic length and velocity. A channel wall does not absorb solute, but will conduct heat, leading to different boundary conditions at the channel wall for solute diffusion (Dirichlet condition) and thermal diffusion (Neumann condition). The theory for a Taylor–Aris-dispersion-like effect in thermal diffusion is not yet completely well-described[29].

### 2.1.6 Equivalent circuit theory

In Eq. (2.10) we notice, that there is a linear relation between the applied pressure,  $\Delta p$ , and the flowrate,  $Q$ . This is a general feature of Poiseuille flow, stemming from the linearity of pressure in Eq. (2.7). The flowrate has dimension  $\mathcal{V}/t$  and the driving pressure difference has dimension  $E/\mathcal{V}$ . Analogous to electrical resistance relating voltage difference (energy pr. charge) and current (flow of charge pr. time) in electrical circuit theory, we can define a hydraulic resistance,  $R_{\text{hyd}}$ , relating applied pressure difference and volumetric flowrate. For the rectangular channel we have,

$$\Delta p = R_{\text{hyd}} Q \quad \text{where} \quad R_{\text{hyd}} \equiv \frac{12\eta L}{1 - 0.630(h/w)} \frac{1}{h^3 w}. \quad (2.29)$$

This hydraulic equivalent to Ohm’s law is called the Hagen–Poiseuille law. Reformulating flow problems in this circuit equivalent manner is a very convenient way to work with flow in complex arrays of channels or in channels with piecewise constant geometry, as we shall see later on. As we see from Eq. (2.23), the Hagen-Poiseuille law is valid in any channel cross-section for low Reynolds-numbers, allowing us to calculate e.g. the total fluidic resistance of connections of fluidic elements in series using regular circuit theory.

## 2.2 Introduction to acoustophoretic separation

Here, we shall briefly introduce the theory of ultrasonic resonances in microfluidic systems and present the physical principles behind the technique of acoustophoretic separation. Acoustic resonances in microfluidic chips are typically set up by attaching a piezo transducer to a microfluidic chip and driving it with a sinusoidal voltage. The varying expansion and contraction of the piezo transducer due to the applied sinusoidal voltage will induce

pressure waves that can propagate throughout the chip. To gain some theoretical insight into the pressure waves in the water channel, we can employ perturbation theory. Due to the need for subscript numbers to denote the perturbation order, we shall some times use regular vector notation in this section.

### 2.2.1 The acoustic wave equations in microfluidics

Consider a water-filled microchannel in a quiescent state, where the water has no motion and is in thermal equilibrium. The relevant physical quantities to consider are the density field,  $\rho$ , the pressure field,  $p$ , and the velocity field,  $\mathbf{v}$ . If we assume that the acoustic fields in the water are a minor perturbation to the quiescent state, we can write the fields,

$$p = p_0 + p_1 + p_2 + \dots, \quad (2.30a)$$

$$\rho = \rho_0 + \rho_1 + \rho_2 + \dots, \quad (2.30b)$$

$$\mathbf{v} = \mathbf{0} + \mathbf{v}_1 + \mathbf{v}_2 + \dots, \quad (2.30c)$$

where we have the zeroth-order fields  $p_0$ ,  $\rho_0$  and  $\mathbf{v}_0 \equiv \mathbf{0}$  in thermal equilibrium and disregard the hydrostatic pressure due to linearity in the equations. We also let the perturbation parameter be implicit. The subscript numbers denote the perturbation order, e.g.  $p_1$  is the the first-order pressure perturbation. We will couple the pressure field and the density field using the thermodynamic relation,  $p = p(\rho)$ , Taylor-expanded around  $\rho_0$ . We keep only terms to second order to get,

$$p = p_0 + c_a^2 \rho_1 + \frac{1}{2} (\partial_\rho c_a^2)_0 \rho_1, \quad (2.31)$$

where we introduce the shorthand notation,  $c_a \equiv (\partial_\rho p)_s$ , for the isentropic derivative. Water is isotropic, so this derivative takes the same value in all spatial directions and we shall see from Eq. (2.42), that  $c_a$  turns out to be the speed of sound. We can already now say, that since the speed of sound is the characteristic velocity of pressure wave propagation, we choose the perturbation parameter  $\epsilon \equiv |\mathbf{v}|/c_a$ .

Inserting Eq. (2.30a)-Eq. (2.30c) into the compressible Navier-Stokes equation, Eq. (2.2), the continuity equation, Eq. (2.3), and the equation of state Eq. (2.31) and collecting only zeroth-order terms yields

$$0 = -\nabla p_0 \quad (2.32)$$

$$\partial_t \rho_0 = 0 \quad (2.33)$$

$$p = p_0. \quad (2.34)$$

We see, that only the constant, quiescent, initial-state fields are solutions to the zeroth-order equations. By collecting only first-order terms, we get

$$\rho_0 \partial_t \mathbf{v}_1 = -c_a^2 \nabla \rho_1 + \eta \nabla^2 \mathbf{v}_1 + \beta \eta \nabla (\nabla \cdot \mathbf{v}_1), \quad (2.35)$$

$$\partial_t \rho_1 = -\rho_0 \nabla \cdot \mathbf{v}_1, \quad (2.36)$$

$$p_1 = c_a^2 \rho_1, \quad (2.37)$$

Table 2.1: Typical parameters for ultrasound waves in water-filled microchannels.

frequency	$f$	$1.0 \times 10^6$ Hz	wavelength	$\lambda$	$1.5 \times 10^{-3}$ m
angular frequency	$\omega$	$6.3 \times 10^6$ rad/s	wave number	$k_0$	$4.2 \times 10^3$ m <sup>-1</sup>
speed of sound	$c_a$	$1.5 \times 10^3$ m/s	damping length	$x_c$	$8.2 \times 10^1$ m
density	$\rho_0$	$1.0 \times 10^3$ kg m <sup>-3</sup>	damping coeff.	$\lambda$	$3.0 \times 10^{-6}$
channel dimension	$L$	$1.0 \times 10^{-4}$ m	piezo amplitude	$\ell$	$1.0 \times 10^{-9}$ m

where we have taken the constant zeroth-order fields out of the differential operators and used the linear relation from Eq. (2.31) to express  $p_1$  in terms of  $\rho_1$ .

Taking the divergence of the first-order Navier-Stokes equation, Eq. (2.35), and inserting the first-order continuity equation, Eq. (2.36), yields a wave equation for the density field,

$$-\partial_t^2 \rho_1 = -c_a^2 \nabla^2 \rho_1 - \frac{(1+\beta)\eta}{\rho_0} \nabla^2 (\partial_t \rho_1). \quad (2.38)$$

We want to describe acoustic resonances due to pressure waves induced by a piezo transducer driven with a sinusoidal voltage, so we seek solutions with a harmonic time dependence,

$$\rho_1 = \rho_1(\mathbf{r})e^{-i\omega t}, \quad (2.39)$$

to get the usual transformation  $\partial_t \rho_1 \rightarrow -i\omega \rho_1$ . This yields

$$\omega^2 \rho_1 = -c_a^2 \left[ 1 - i \frac{(1+\beta)\eta\omega}{\rho_0 c_a^2} \right] \nabla^2 \rho_1 = -c_a^2 [1 - i2\gamma] \nabla^2 \rho_1, \quad (2.40)$$

where we have introduced the acoustic damping factor,  $\gamma$ , a frequency-dependent, complex term leading to exponential decay in the water. Using typical parameters for ultrasound waves in water-filled microchannels from Table 2.1, we get

$$\gamma(\omega) \equiv \frac{(1+\beta)\eta\omega}{2\rho_0 c_a} \approx 10^{-5} \ll 1. \quad (2.41)$$

Due to the smallness of  $\gamma$ , we can approximate  $[1 - i2\gamma] \approx [1 + i\gamma]^{-2}$  and rewrite Eq. (2.40) as a Helmholtz wave equation for a damped wave,

$$\nabla^2 \rho_1 = - \left[ \frac{\omega}{c_a} (1 + i\gamma) \right]^2 \rho_1 = - [k_0 (1 + i\gamma)]^2 \rho_1 = -k^2 \rho_1, \quad (2.42)$$

where we have introduced the real-valued wave number,  $k_0 \equiv \omega/c_a$  and the complex wave number  $k \equiv k_0(1 + i\gamma)$ . From this equation, we can in fact see, that  $c_a$  indeed is the propagation velocity of the pressure waves, i.e. the speed of sound in water, see Table 2.1.

If we assume a rotation free first-order velocity field, we can introduce a first-order velocity potential  $\phi_1$ , so that  $\mathbf{v}_1 = \nabla \phi_1$ . Just like for  $\rho_1$ , we seek solutions with harmonic time dependences;  $p_1 = p_1(\mathbf{r})e^{-i\omega t}$  and  $\phi_1 = \phi_1(\mathbf{r})e^{-i\omega t}$ . By using the linear relation

between  $p_1$  and  $\rho_1$  from the first-order equation of state, Eq. (2.37), and rewriting the first-order continuity equation, Eq. (2.36), as  $\nabla \cdot \mathbf{v}_1 = \nabla^2 \phi_1 = -(\partial_t \rho_1)/\rho_0 = i\omega \rho_1/\rho_0$ , it is straightforward to show that we also have damped Helmholtz wave equations for  $\rho_1$  and  $\phi_1$ .

### 2.2.2 Setting up acoustic resonances

Having showed, that we can derive wave equations for  $\rho_1$ ,  $p_1$  and  $\phi_1$ , we can now turn our attention towards the actual problem of the acoustic resonances. Resonant modes will be eigenvalues to the damped Helmholtz wave equation. When looking for solutions in the water domain, we have two distinct types of boundary conditions on the pressure field; (i) the so-called *soft wall*, a Dirichlet boundary condition where we require that the pressure be zero at the wall,

$$p_1 = 0, \quad (2.43)$$

and (ii) the so-called *hard wall*, a Neumann boundary condition where we require that the spatial derivative along the direction of the normal is zero,

$$\mathbf{n} \cdot \nabla p_1 = 0. \quad (2.44)$$

From regular macroscopic acoustic wave mechanics, we know, that in some rectangular water domain (channel) of length  $L$ , width  $w$  and height  $h$ , there will exist resonant modes that satisfy,

$$\omega^2 = c_a^2 \left[ \left( \frac{2\pi l}{L} \right)^2 + \left( \frac{2\pi m}{w} \right)^2 + \left( \frac{2\pi n}{h} \right)^2 \right], \quad (2.45)$$

where we have introduced the wave numbers  $(l, m, n) \in \mathbb{N}^3$ . If we define a cartesian coordinate system with  $x$  along the channel length,  $y$  along the channel width and  $z$  along the channel height, we have that pure soft walls give  $p_1$  as a product of sines,

$$p_1 = p_a \sin \left( \frac{\pi l}{L} x \right) \sin \left( \frac{\pi m}{w} y \right) \sin \left( \frac{\pi n}{h} z \right), \quad (2.46)$$

and pure hard walls give  $p_1$  as a product of cosines,

$$p_1 = p_a \cos \left( \frac{\pi l}{L} x \right) \cos \left( \frac{\pi m}{w} y \right) \cos \left( \frac{\pi n}{h} z \right), \quad (2.47)$$

where  $p_a$  is some pressure amplitude.

As previously mentioned, we usually set up the pressure resonances in microsystems with a harmonically oscillating piezo actuator. Usual channel dimensions in microfluidics are on the order of hundreds of micrometers and the oscillation amplitude of a piezo actuator is on the order of few nanometers. For simplicity, we consider a symmetric setup with a piezo on both sides of the water-channel. To catch the basic physics of the resonant build-up in this case, we can consider a water domain of length  $2L$  between two infinite parallel walls. To model the piezo actuation, we impose the boundary condition on the first-order velocity field, that it must vary with a harmonic time-dependence and with a

characteristic velocity  $\omega\ell$ , where  $\omega$  is the piezo frequency and  $\ell \ll L$  is some small piezo amplitude,  $v_1(\pm L, t) = \pm\omega\ell e^{-i\omega t}$ . We seek solutions where the velocity potential,  $\phi_1$ , is a superposition of counterpropagating plane waves,

$$\phi_1(x, t) = \left[ Ae^{ikx} + Be^{-ikx} \right] e^{-i\omega t}, \quad (2.48)$$

where  $k \equiv k_0(1 + i\gamma)$  is the complex wave-number. Taking the gradient of  $\phi_1$  to find  $v_1$  and inserting into the continuity equation, Eq. (2.36), to find  $\rho_1$  yields

$$v_1(x, t) = \partial_x \phi_1 = ik \left[ Ae^{ikx} + Be^{-ikx} \right] e^{-i\omega t}, \quad (2.49a)$$

$$\rho_1(x, t) = -\frac{\rho_0 k^2}{\omega^2} \partial_t \phi_1 = i \frac{\rho_0 k^2}{\omega} \left[ Ae^{ikx} + Be^{-ikx} \right] e^{-i\omega t}. \quad (2.49b)$$

To satisfy the boundary conditions, we see that  $A = B = -\omega\ell/2k \sin(kL)$ . By inserting this back into Eq. (2.49a)-Eq. (2.49b) and utilizing the smallness of  $\gamma k_0 L \ll 1$  to Taylor expand in  $k$  around  $k_0$ , we arrive at the approximate expressions for  $\phi_1$ ,  $v_1$  and  $\rho_1$ , where  $v_1$  is

$$v_1(x, t) = \omega\ell \frac{\sin(kx)}{\sin(kL)} e^{-i\omega t} \approx \omega\ell \frac{\sin(k_0 x) + i\gamma k_0 x \cos(k_0 x)}{\sin(k_0 L) + i\gamma k_0 L \cos(k_0 L)}. \quad (2.50)$$

We see, that in the general, off-resonance case, the order of magnitude of the fields are given by the prefactors, so that  $|v_1(x, t)| \approx \omega\ell = (\omega\ell/c_a)c_a$ , where we can explicitly read off the the perturbation parameter  $\omega\ell/c_a \approx 10^{-6}$ , given that we use typical parameters from Table 2.1. More interestingly, we see that due to the  $\sin(k_0 L)$ -term in the denominator, there will exist solutions, where the piezo actuation frequency matches the channel dimension so that  $\sin(k_0 L) = 0$  leading to a blow-up of the equations, i.e. a resonant mode. As expected from Eq. (2.46) and Eq. (2.47), we have the resonance condition,  $k_0 = n\pi/L$ . At resonance, the  $v_1$  reduces to

$$v_1(x, t) \approx \omega\ell \left[ \frac{-i}{n\pi\gamma} \sin\left(n\pi \frac{x}{L}\right) + \frac{x}{L} \cos\left(n\pi \frac{x}{L}\right) \right] e^{-i\omega t}, \quad (2.51)$$

allowing us to read off the order of magnitude of the resonant fields, e.g.

$$|v_1(x, t)| \approx \frac{1}{n\pi\gamma} \frac{\omega\ell}{c_a} c_a \approx 3 \times 10^{-2} c_a, \quad (2.52)$$

which is four orders of magnitude larger than the off-resonance fields. This is borderline invalidating the whole perturbation approach, but we have qualitatively shown what we wanted, namely, that it is possible to set up resonant pressure modes in water-microchannels by piezo actuation with ultrasound frequencies.

### 2.2.3 Modelling resonances in actual microchips

In real microsystems, we do not have isolated water domains, but rather water channels in some chip usually constructed from glass, silicon or some glassy polymer like PMMA,

Table 2.2: Acoustic properties of typical Lab-on-a-chip materials.

	$\rho_0$ kg/m <sup>3</sup>	$c_a$ m/s	$Z = \rho_0 c_a$ kg/(m <sup>2</sup> s)
air	1.16	343.4	$3.99 \times 10^5$
water	998	1483	$1.48 \times 10^6$
silicon	2331	8490	$1.98 \times 10^7$
pyrex glass	2230	5640	$1.25 \times 10^7$
PDMS	965	1076[28]	$3.99 \times 10^5$
PMMA	1190	1588[25]	$1.89 \times 10^6$

The rest of the parameters are from [17]

with a piezo actuator attached to the outside of the chip. Different materials have different acoustic properties, see Table 2.2, so we will need to consider the transmission of waves across material interfaces. Consider a 1D geometry with an interface at  $x_0$  between two infinite parallel materials  $a$  and  $b$ . We require, that the first-order velocity and pressure fields be continuous at interfaces.

$$v_a(x_0, t) = v_b(x_0, t), \quad (2.53)$$

$$p_a(x_0, t) = p_b(x_0, t). \quad (2.54)$$

Utilizing the continuity of  $\omega$  throughout the device and expressing  $v_1$  in terms of  $p_1$  and  $\rho_0$ , we can reformulate this in terms of the only the first-order pressure and zeroth-order density fields,

$$p_a(x_0, t) = p_b(x_0, t), \quad (2.55)$$

$$\frac{1}{\rho_a} \mathbf{n} \cdot \nabla p_a(x_0, t) = \frac{1}{\rho_b} \mathbf{n} \cdot \nabla p_b(x_0, t). \quad (2.56)$$

In this thesis, we shall specifically consider water chip structures with water channels in glass chips. In the general case, it is necessary to describe the acoustic fields in the solid chip materials using theory of elasticity and couple them to the acoustic fields in the water channels at the channel wall interfaces, but due to the amorphousness of glass, we shall mathematically treat the glass domains as an isotropic fluid.

#### 2.2.4 Second order effects: Acoustic forces

Having shown, that we can establish resonant modes with standing waves in the acoustic fields in water-filled microchannels, we now turn our attention to the effects these fields have on particles suspended water. In lab-on-a-chip systems, these particles would typically be biologicals cells, vesicles or polystyrene beads (e.g. microbeads labelled with an antibody for some bio-detection) with a radius  $a$  on the order of micrometers.

We have seen, that the piezo actuation induces a velocity field in the water. To describe this effect more accurately, we have to turn to laminar boundary theory. We shall not

present the full calculations here, but basically, in the boundary layer theory, the Navier–Stokes equation reduces to Prandtl’s so-called incompressible boundary layer equations. Going to second-order in these equations, it turns out that on time-average, the piezo actuation induces a bulk motion in the liquid. Because it is a boundary-layer effect, it is closely associated with the geometry of the channel, and can take on interesting geometric shapes e.g. induce flow rolls[26]. This is known as *acoustic streaming*. Intuitively, we can say, that if the suspended particles are very small, they will follow the induced flow patterns due to Stokes drag. On the other hand, it is also intuitive, that if the suspended particle has a size comparable to the gradients in the standing pressure fields, the incoming pressure wave will result in a net force on the particle

Since we have micrometer-sized particles,  $a \ll \lambda$ , the proper mathematical approach to calculating the acoustic radiation force is to treat it as a radiation force due to scattering of the acoustic wave on a point particle. The time-average of the first-order acoustic fields vanishes, so we have to consider second-order fields  $p_2$ ,  $\rho_2$  and  $\mathbf{v}_2$ . Inserting the perturbation series, Eq. (2.30a)-Eq. (2.30c), into the compressible Navier-Stokes equation, Eq. (2.2), and collecting only second-order terms yields

$$\rho_1 \partial_t \mathbf{v}_1 + \rho_0 \partial_t \mathbf{v}_2 + \rho_0 (\mathbf{v}_1 \cdot \nabla) \mathbf{v}_1 = -\nabla p_2 + \eta \nabla^2 \mathbf{v}_2 + \beta \eta \nabla (\nabla \cdot \mathbf{v}_2), \quad (2.57)$$

disregarding effects from viscosity,  $\eta \approx 0$ , and taking the time average leaves us with

$$\nabla \langle p_2 \rangle = -\langle \rho_1 \partial_t \mathbf{v}_1 \rangle - \rho_0 \langle (\mathbf{v}_1 \cdot \nabla) \mathbf{v}_1 \rangle. \quad (2.58)$$

We still assume no rotation in  $\mathbf{v}_1$ , so using the first-order continuity equation, Eq. (2.36), and the Taylor-expanded equation of state, Eq. (2.37), we can rewrite Eq. (2.58) as a sum of pressure fluctuations and the negative Bernoulli effect

$$\langle p_2 \rangle = \frac{1}{2\rho_0 c_a^2} \langle p_1^2 \rangle - \frac{1}{2} \rho_0 \langle v_1^2 \rangle. \quad (2.59)$$

Now consider the momentum  $\mathbf{P}(\Omega, t)$  in some small domain  $\Omega$  encompassing a scattering particle. The acoustic radiation force on the particle can be found by considering conservation of momentum. The total rate of change of momentum must be

$$\partial_t \mathbf{P}(\Omega, t) = \partial_t \int_{\Omega} d\mathbf{r} \rho(\mathbf{r}, t) \mathbf{v}(\mathbf{r}, t). \quad (2.60)$$

The change of momentum due to the second-order pressure field must be

$$\partial_t \mathbf{P}(\Omega, t) = - \int_{\partial\Omega} d\mathcal{A} \langle p_2 \rangle \mathbf{n}, \quad (\text{pressure}) \quad (2.61)$$

and the change of momentum due to momentum flux can be found by expressing the momentum flux density in terms of  $\mathbf{v}_1$ , so  $\mathbf{J} = \rho_0 \langle \mathbf{v}_1 \mathbf{v}_1 \rangle$ , yielding

$$\partial_t \mathbf{P}(\Omega, t) = - \int_{\partial\Omega} d\mathcal{A} \mathbf{n} \cdot (\rho_0 \langle \mathbf{v}_1 \mathbf{v}_1 \rangle). \quad (\text{momentum flux}) \quad (2.62)$$

Using Gauss' theorem to rewrite Eq. (2.60) as a surface integral, combining with Eq. (2.61) and Eq. (2.62), and using that  $\mathbf{F}_{\text{ac}} = \partial_t \mathbf{P}$  yields an expression for the acoustic radiation force,

$$\mathbf{F}_{\text{ac}} = - \int_{\partial\Omega} d\mathcal{A} \left\{ \left[ \frac{1}{2\rho_0 c_a^2} \langle p_1^2 \rangle - \frac{1}{2} \rho_0 \langle v_1^2 \rangle \right] \mathbf{n} + \rho_0 \langle (\mathbf{n} \cdot \mathbf{v}_1) \mathbf{v}_1 \rangle \right\}. \quad (2.63)$$

By re-introducing the velocity potential  $\phi_1$ , so  $\mathbf{v}_1 = \nabla \phi_1$ , the scattering potential from the particle can be calculated by multipole expansion, which was done very eloquently by Gorkov[7]. We shall not go through the derivation here, but it turns out that we can express the acoustic radiation force  $\mathbf{F}_{\text{ac}}$  acting on a small particle ( $a \ll \lambda$ ) in an arbitrary acoustic field in terms of an acoustic radiation potential  $U_{\text{ac}}$ ,

$$\mathbf{F}_{\text{ac}} = -\nabla U_{\text{ac}} \quad (2.64)$$

$$U_{\text{ac}} = \frac{4\pi}{3} a^3 \left[ f_1 \frac{1}{2\rho_0 c_a^2} \langle p_{\text{in}}^2 \rangle - f_2 \frac{3}{4} \rho_0 \langle v_{\text{in}}^2 \rangle \right] \quad (2.65)$$

$$f_1 = 1 - \frac{\rho_0 c_a^2}{\rho_p c_p^2} \quad f_2 = \frac{2(\rho_p - \rho_0)}{2\rho_p + \rho_0} \quad (2.66)$$

where  $p = \text{in}$  and  $v_{\text{in}}$  are the incoming first-order acoustic fields from the wave. We see from the prefactors  $f_1$  and  $f_2$  that the force vanishes if the densities,  $\rho_{p(0)}$ , and speeds of sound,  $c_{p(a)}$ , of the particle(water) are equal and see from the prefactor in Eq. (2.65), that the magnitude of the force scales with the particle volume making the acoustic radiation force the dominant force on larger particles. We can also see, that depending on the ratio between the two terms in Eq. (2.65),  $\mathbf{F}_{\text{ac}}$  can change sign and move the particle either up or down the potential. The actual cross-over particle size where the radiation force becomes important can be estimated by comparing the order of magnitude of radiation force to the order of magnitude of the Stokes drag due to the streaming velocity and turns out to yield a cross-over radius  $a \approx 1 \mu\text{m}$ [6].

### 2.2.5 Acoustophoresis in resonant microchannels

For application to acoustophoretic separation, we consider a water-filled microchannel with a transverse, standing, resonant, half-wavelength, plane ultrasound pressure wave as in Fig. 2.3. If we have tharmonic time-dependece  $\sin(\omega t)$  of the pressure wave, we can write the incoming pressure from the wave

$$p_{\text{in}} = p_a \cos(ky) \sin(\omega t) \quad (2.67)$$

where  $p_a$  is the first-order pressure amplitude and we disregard viscosity to the real-valued wave number  $k = \omega/c_a = 2\pi/\lambda$ . From translational invariance along the channel, we see that the force only has a  $y$ -component,  $\mathbf{F}_{\text{ac}} = F_{\text{ac}} \mathbf{e}_z$ , and by determining the first-order velocity field from the first-order equations and inserting into Eq. (2.65), we can find the acoustic radiation force,

$$F_{\text{ac}} = 4\pi a^2 (ka) E_{\text{ac}} \Phi \sin(2ky), \quad (2.68)$$

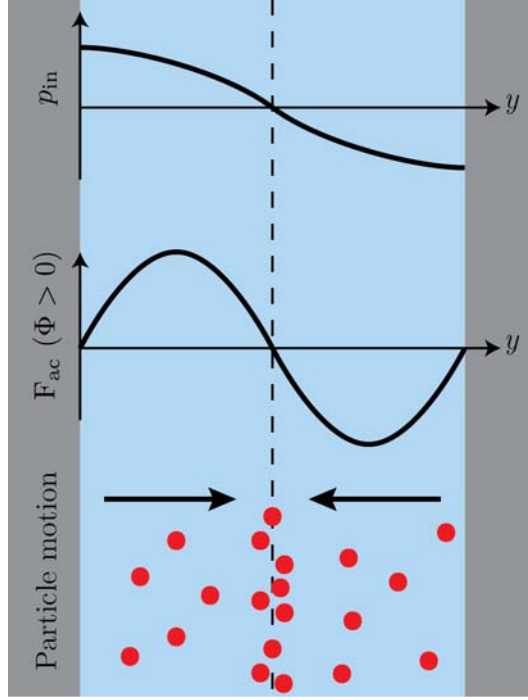


Figure 2.3: End view of straight water-filled microchannel (grey walls) with a transverse standing ultrasound resonant half-wavelength plane pressure wave (black half cosine wave, top). The acoustic radiation force is period doubled and phase shifted (black full sine wave, middle) leading to motion of suspended microparticles towards central nodal line (red spheres, bottom).

where we have introduced the the so-called acoustophoretic contrast factor,  $\Phi$ , and the acoustic energy density in the standing wave  $E_{ac}$ ,

$$\Phi = \frac{\rho_p + \frac{2}{3}(\rho_p - \rho_0)}{2\rho_p + \rho_0} - \frac{1}{3} \frac{\rho_0 c_a^2}{\rho_p c_p^2}, \quad (2.69)$$

$$E_{ac} = \frac{1}{4} \rho_0 u_0^2 = \frac{p_a^2}{4\rho_0 c_a^2}, \quad (2.70)$$

where we express the pressure amplitude in terms of the zeroth-order density,  $\rho_0$ , and the velocity amplitude  $u_0$  so  $p_a = \rho_0 c_a u_0$ . We notice a period-doubling in Eq. (2.68), so we get a full wave in the pressure field, as shown in Fig. 2.3. Depending of the sign of  $\Phi$ , particles in the channel will either move towards the walls ( $\Phi < 0$ ) or towards the central nodal line ( $\Phi > 0$ ). Due to Stokes drag, the particles will move with a velocity proportional to the force and a typical magnitude of the force can be calculated from typical values of the energy density. For low-voltage ( $\lesssim 10$  V) piezo actuation at a few MHz,  $E_{ac} \approx 10 - 100 \text{ J m}^{-3}$ [3].

Using the acoustic radiation force to separate particles in a sample flow in the microchannel has been dubbed *acoustophoresis*. Consider a channel with a bulk flow of buffer

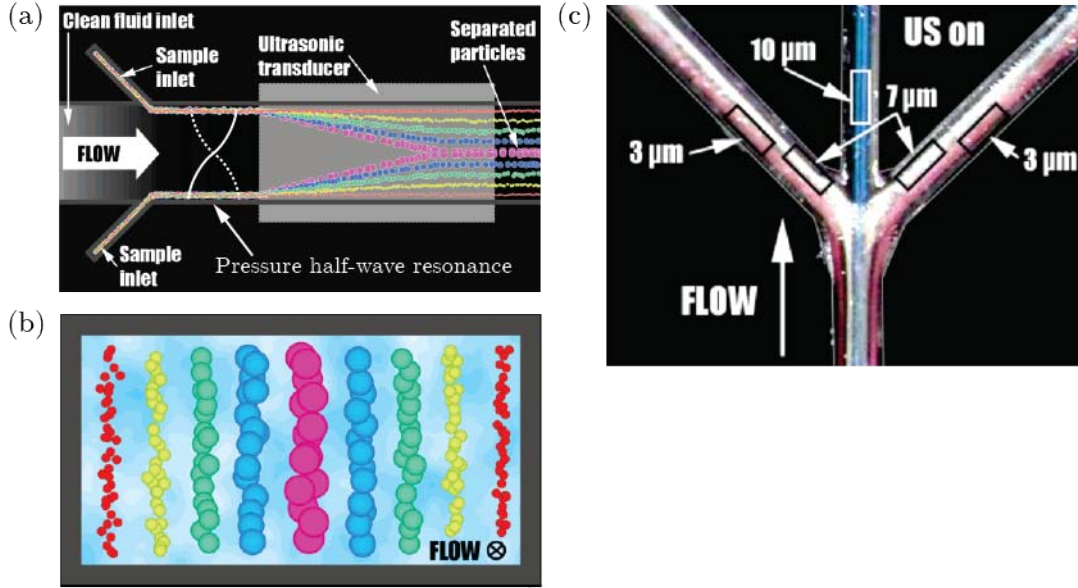


Figure 2.4: (a) Illustration of a particle suspension passing over the transducer where the particles are moved toward the center of the separation channel at a rate determined by their acoustic properties. Because of the laminar flow almost no mixing takes place. (b) Cross-sectional view of the separation channel after acoustophoretic separation. The piezo voltage (i.e. actuation amplitude) is tuned, so the largest particles are moved to the center of the channel in the channel traverse time, while the others are located somewhere between the walls and the center. (c) Actual separation of 3  $\mu\text{m}$  (red), 7  $\mu\text{m}$  (white) and 10  $\mu\text{m}$  (blue) beads using a trifurcation to separate the laminar outflow from the channel. Channel is 370  $\mu\text{m}$  wide and 125  $\mu\text{m}$  deep and the total sample flowrate is 2.4 mL/min. Figures adapted from Petersson *et. al.* 2007 [22]

and an inflow of sample containing microparticles at the channel walls, as in Fig. 2.4(a). By setting up a standing, antisymmetric half-wave acoustic resonance in the channel, the particles in the sample flow will be subject to the acoustic radiation force. Assuming a positive contrast factor, all particles will be moved towards the central nodal line, but from Eq. (2.68), we see that due to differences in the acoustic contrast factor,  $\Phi$ , and size,  $4\pi a^2$ , the magnitude of the force will be different on different types of particles. Utilizing the fact, that the particles traverse the microchannel in a finite time we can separate the particles in distinct bands in the flow based on volume and acoustic contrast factor. Fig. 2.4(c) shows actual separation of polystyrene based on size by free-flow alignment into bands with a trifurcation acting as a simple hi-pass-filter for  $\mathbf{F}_{ac}$ , by Petersson *et. al.* 2007[22].

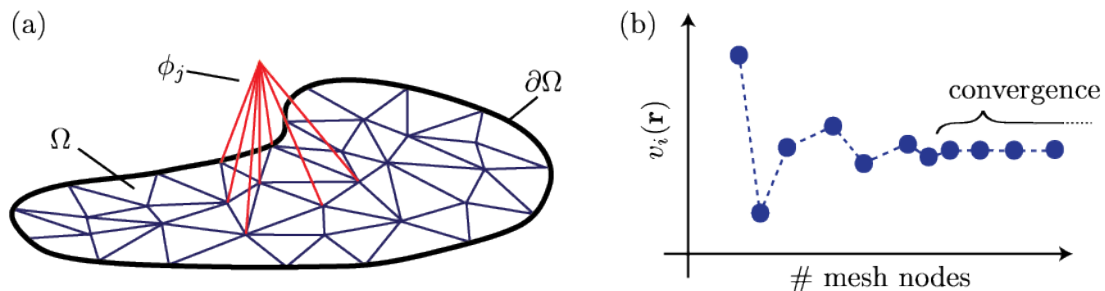


Figure 2.5: (a) Example of triangular mesh structure (blue lines) on some domain,  $\Omega$ , showing a linear basis function,  $\phi_j$  (red lines) being unity at one node and decaying linearly to zero on the links between neighboring nodes. (b) Example of convergence analysis for some quantity  $v_i(\mathbf{r})$  showing that for an increasing number of mesh nodes, the mesh will eventually be fine enough to sufficiently mesh the domain and make the finite element model converge.

## 2.3 Introduction to finite element method solutions.

To calculate various physical fields in the acoustophoretic device in the thesis, we shall sometimes use finite element analysis. The finite element analysis in this thesis is done with MATLAB in conjunction with the software package COMSOL *Multiphysics* and with the standalone COMSOL GUI. To find a solution of a vector field  $\mathbf{v}(\mathbf{r}, t)$  for some partial differential equation in some domain  $\Omega$ , the domain is discretized to a so-called *mesh* consisting of a finite number of finite-sized triangular elements, see Fig. 2.5(a). We introduce a finite set of  $N$  basis functions  $\phi_j$  and seek solutions on the form,

$$v_i(\mathbf{r}) \approx \sum_{j=1}^N v_j^{(i)} \phi_j(\mathbf{r}). \quad (2.71)$$

where we solve for the coefficients  $v_j^{(i)}$ . The  $j$ 'th basis function has the property of only being non-zero in elements neighboring the  $j$ 'th node  $\mathbf{r}_j$ . At  $\mathbf{r}_j$  itself,  $\phi_j(\mathbf{r}_j) \equiv 1$ , and  $\phi_j$  decays continuously to zero at the links between the neighboring nodes; See Fig. 2.5(a) for a sketch of a basis function with a linear decay. COMSOL provides a very nice framework for numerically computing solutions to partial differential equations in arbitrary domains with arbitrary boundary conditions using finite element methods with built-in algorithms for meshing and solving.

In the general case, any partial differential equation for the  $m$ 'th dependent variable in in some domain  $\Omega$  can be written,

$$d_m \frac{\partial u_m}{\partial t} + \nabla \cdot \mathbf{\Gamma}_m = f_m, \quad \forall \mathbf{r} | \mathbf{r} \in \Omega, \quad (2.72)$$

where  $u_m$  is the dependent variable, and the coefficient  $d_m$ , the flux vector  $\mathbf{\Gamma}_m$  and the source field  $f_m$  are some arbitrary functions of  $\mathbf{r}$ ,  $t$  or dependent variables. Higher-order derivatives can be achieved by using Eq. (2.72) in series and defining some dependent

variable as the derivative of another variable. Using COMSOL, we can mesh the domain  $\Omega$  and solve numerically for  $u_m$ , subject to two boundary conditions at the boundary  $\partial\Omega$ , simultaneously,

$$R_m = 0, \quad \forall \mathbf{r} | \mathbf{r} \in \partial\Omega \quad (2.73a)$$

$$-\mathbf{n} \cdot \mathbf{\Gamma}_m = G_m + \mu_k \frac{\partial R_k}{\partial u_m}, \quad \forall \mathbf{r} | \mathbf{r} \in \partial\Omega \quad (2.73b)$$

where  $\mathbf{n}$  is the normal vector to the boundary,  $\mu_k$  is a Lagrange multiplier for the  $k$ 'th boundary element and  $G_m$ ,  $R_m$  and  $R_k$  are some functions of  $\mathbf{r}$ ,  $t$  or dependent variables. If  $\partial R_k / \partial u_m \neq 0$ , the Lagrange multiplier,  $\mu_k$  is chosen so that Eq. (2.73b) is satisfied. For instance, if we choose,

$$\mathbf{\Gamma} = \begin{bmatrix} \partial_x p \\ \partial_y p \\ \partial_z p \end{bmatrix}, \quad d_m = 0 \quad f = -k^2 p, \quad G = 0, \quad R = p, \quad (2.74)$$

and insert, we see that we get the Helmholtz wave equation for pressure with a hard-wall Dirichlet boundary condition.

*Convergence analysis* is an extremely important part of using finite element methods. When meshing the domain  $\Omega$  it is crucial that the mesh is fine enough for the finite set of basis functions to fully resolve the domain geometry. If the mesh is not fine enough, numerical solutions on the mesh may converge, but the solution is not an accurate approximation to the solution to the actual domain. When calculation some quantity on the mesh,  $v_i(\mathbf{r})$ , one must always find converging solutions for increasingly fine meshes to make certain, that the solution as a function of number of mesh nodes has indeed converged to an accurate approximation to the solution on the actual domain, see Fig. 2.5(b).

In the thesis, we shall not go into great detail of how the fields are actually solved using MATLAB and COMSOL, since this is essentially a mundane programming task and provides the reader with no interesting physical insight. We shall restrict ourselves to discussing the physical models, i.e. bulk equations and boundary conditions. For all results calculated using finite element methods in this thesis, convergence analysis has been performed to make sure that the mesh was sufficiently fine.

## Chapter 3

# High-throughput device

### 3.1 Introduction to high-throughput design

Here we present a microfluidic device capable of high-throughput, continuous-flow acoustophoretic separation of cells and microparticles. The device is easily and rapidly fabricable from low-cost materials readily available in most labs without the use of time-consuming clean room techniques. Constructing the device in this low-cost, rapid-prototyping manner has some novelty value, but it also makes the device design easy to copy and manufacture in other laboratories. This facilitates easy application and integration of high-throughput acoustophoretic separation in other laboratories.

Our device consists of one broad microchannel with two inlets and two outlets, in the top and the bottom of the channel, respectively, see Fig. 3.1. We inject a buffer solution of DI water with 0.01  $v/v$  % tween20 (dubbed *buffer flow*) into the top inlet and a buffer solution containing suspended microparticles (dubbed *sample flow*) in the bottom inlet at a flowrate ratio  $Q_{\text{buffer}}/Q_{\text{sample}} = 3$ . In the microchannel, we have a thin glass divider, dividing the flow at the inlet and outlets ends. The flow divider is offset towards the bottom. As we shall later show, due to the low Reynolds number in the device, the flow will be laminar, and no mixing of the buffer and sample sheath flows will occur. This means, that in the absence of any external forces, all sample particles leaving the device through the bottom outlet. When setting up a transverse, standing, resonant, half-wavelength, plane ultrasound pressure wave in the channel by actuation with a piezo transducer, the particles will move towards the central nodal line due to the acoustic radiation force. As shown in the introductory theory, the largest particles will move towards the nodal line with the greatest velocity, allowing us to use the device as a simple high-pass filter for particle size; To a good approximation, the piezo transducer is a linear element, meaning that there is a linear relation between between the applied voltage,  $V$ , amplitude and the piezoelectric response amplitude,  $\ell$ . From Eq. (2.51) we know that the channel pressure  $p \propto \ell$ , and from Eq. (2.68) and Eq. (2.70), we know that  $F_{\text{ac}} \propto p^2$ . This means that  $F_{\text{ac}} \propto V^2$ , so by adjusting  $V$ , we can control the magnitude of  $F_{\text{ac}}$ , so some larger particles are moved to the sheath flow going above the flow divider in the channel traverse time, while other smaller particles are not, thus achieving particle

sparation based on size.

What sets our design apart from similar designs already reported in the literature is the capability for very high throughput. Normally, the acoustic half-wave resonance is set up in the widest dimension of the channel cross-section[27, 1, 16, 19, 10, 23, 14]. Using ultrasonic frequencies in the MHz regime, this limits the widest dimension of the microchannel to approximately a millimeter. This gives a very small cross-sectional area of the channel, limiting the throughput severely, see Fig. 3.2. The conventional setup is very nice to work with, because the resonant mode is in the same plane as the microchip, making it easy to see if the device is on or off resonance with a microscope. Furthermore, because the channel height is so small compared to the wavelength, there are no effects from axial modes in the height dimension. A drawback of the conventional design is that it requires time-consuming and tedious clean room fabrication. The high-throughput design is very easy to fabricate, but is much more difficult to work with. Because the height is the smallest dimension in our device, we have much greater influence from the resonant modes along the length and width of the channel, especially if the device symmetry is somehow broken<sup>1</sup>. Furthermore, the resonance is perpendicular to the plane of the channel, so it is impossible to see directly, if the chip is on or off resonance by looking with a regular microscope. In the literature, only one design with a broad channel like ours has been reported[11]. The device was constructed from PDMS and micromachined brass and steel, and the separation efficiency was not very good ( $\approx 70\%$ ) leading the author to propose the device be used as a kind of micromixer.

## 3.2 Device fabrication

### 3.2.1 Preparation

In the course of the experiments, two slightly different device designs were used. We shall call these the *first-generation* and *second-generation devices*, respectively. The devices were fabricated from layers of PDMS and borosilicate glass, see Fig. 3.3(a). The device layers were drawn in AutoCAD and exported as .dxf-files for use with plotting cutter and computed numerically controlled (CNC) drill. The thick glass reflectors are made from standard 25 mm  $\times$  75 mm, 1.2 mm thick microscope slides. The microscope slides were bonded to a 500  $\mu$ m silicon wafer using crystalbond at  $\sim 155$  °C and the inlet and outlet holes were drilled with a 1.1 mm diamond drill bit in a CNC drill. The slides were removed from the wafer by reheating to  $\sim 155$  °C and cleaned with acetone and isopropanol, successively, before drying with compressed nitrogen. The thin glass divider was diced to 25 mm  $\times$  75 mm from a 170  $\mu$ m glass wafer using an automated dicing saw and bonded to a 500  $\mu$ m silicon wafer using crystalbond at  $\sim 155$  °C. The square cutout was made by slightly modifying the CNC drill code to mill along the dashed path in Fig. 3.3(a) at 2 mm/min. The divider was removed from the wafer by reheating to  $\sim 155$  °C and cleaned with acetone and isopropanol, successively, before drying with compressed nitrogen. A very thin glass divider is desirable, so for the second generation

---

<sup>1</sup>which it will be, as perfect alignment of layers, perfect attachment of piezo actuators, etc. is impossible.

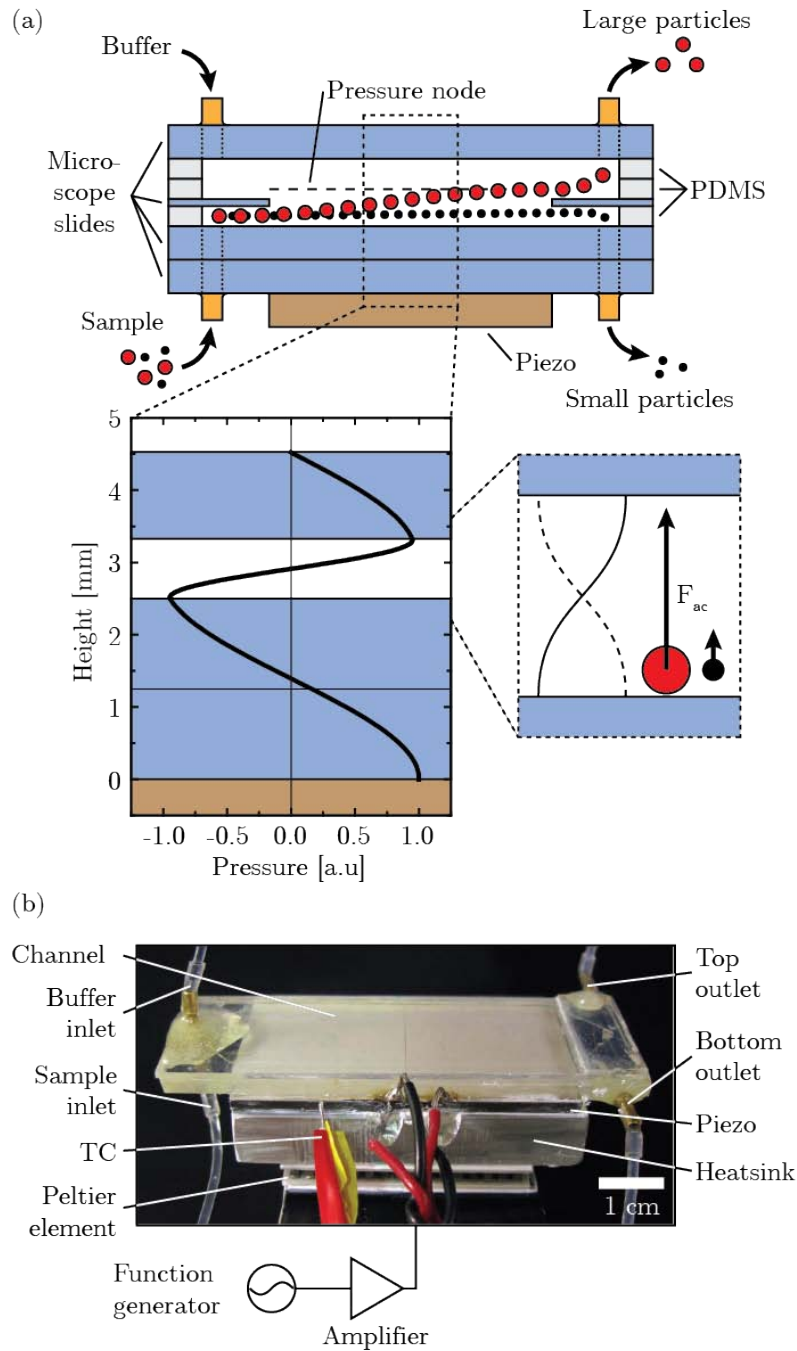


Figure 3.1: (a) Design schematic of the high-throughput device showing pressure resonance (black line) and acoustic radiation force (black arrows). The geometry of the device is designed to support a standing half-wave in the pressure field across the height of the microchannel. (b) The device is mounted in a stable fluidic setup with 500  $\mu\text{m}$ -diameter teflon tubing. The hydraulic resistance (length) of the outlet tubing is matched to ensure a correct outlet flow ratio. The temperature of the device is measured using a chromel/alumel thermocouple (TC). The device is mounted in thermal compound on an aluminum heat sink and cooled by a Peltier element.

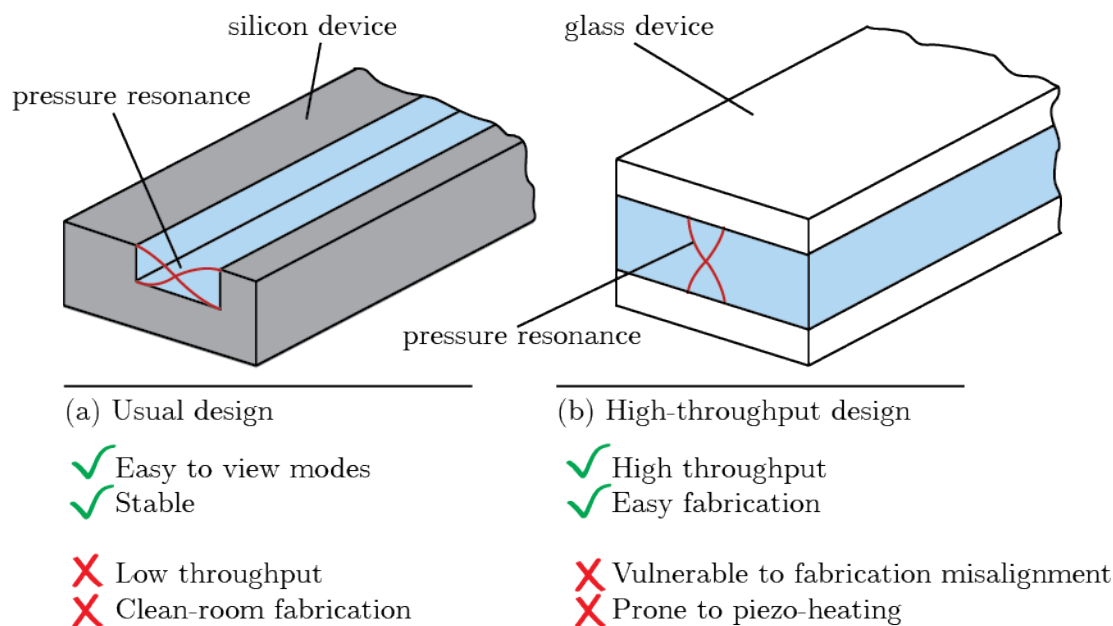


Figure 3.2: Pros and cons of (a) typical acoustophoretic device designs reported in the literature and (b) the high-throughput design presented in this thesis.

device, the thin glass was etched to  $\sim 70 \mu\text{m}$  with HF etch prior to milling. This step could easily be eliminated from the fabrication process by simply purchasing a thinner glass wafer<sup>2</sup>. The PDMS gaskets were cut from 250  $\mu\text{m}$  PDMS sheets using a commercial plotting cutter.

### 3.2.2 Assembly

A short summary of the device assembly is shown in Fig. 3.4. The device layers were bonded in layers as shown in Fig. 3.3(b) and Fig. 3.3(c). Design-improvements in the second generation device are asymmetric glass reflectors to better support the acoustic resonance and a thinner glass flow divider to offset the divider more from the pressure node and to minimize viscous effects on the flow streamlines, see Fig. 3.3(b) and Fig. 3.3(c). Glass and PDMS layers were plasma bonded. To achieve the asymmetric glass reflector setup of the second-generation device, two identical glass reflectors (Fig. 3.3(a), top) were bonded with good acoustic coupling. We investigated bonding two glass slides using anodic bonding and cyanoacrylate superglue, but found the best solution to be a thin layer of epoxy resin. From examination with the microscope, the epoxy layer was estimated to be  $\sim 100 \mu\text{m}$ .

0.045 inch (1.143 mm) brass connectors were attached at the inlets and outlets and set in epoxy resin, see Fig. 3.1(b). A very nice design feature was added to the second-

<sup>2</sup>which we have done. For the third generation design, we will just use a 50  $\mu\text{m}$  glass wafer. This is nice, because etching the glass down leads to some surface roughness and, as we have observed, makes particles in the flow stick very much to the divider.

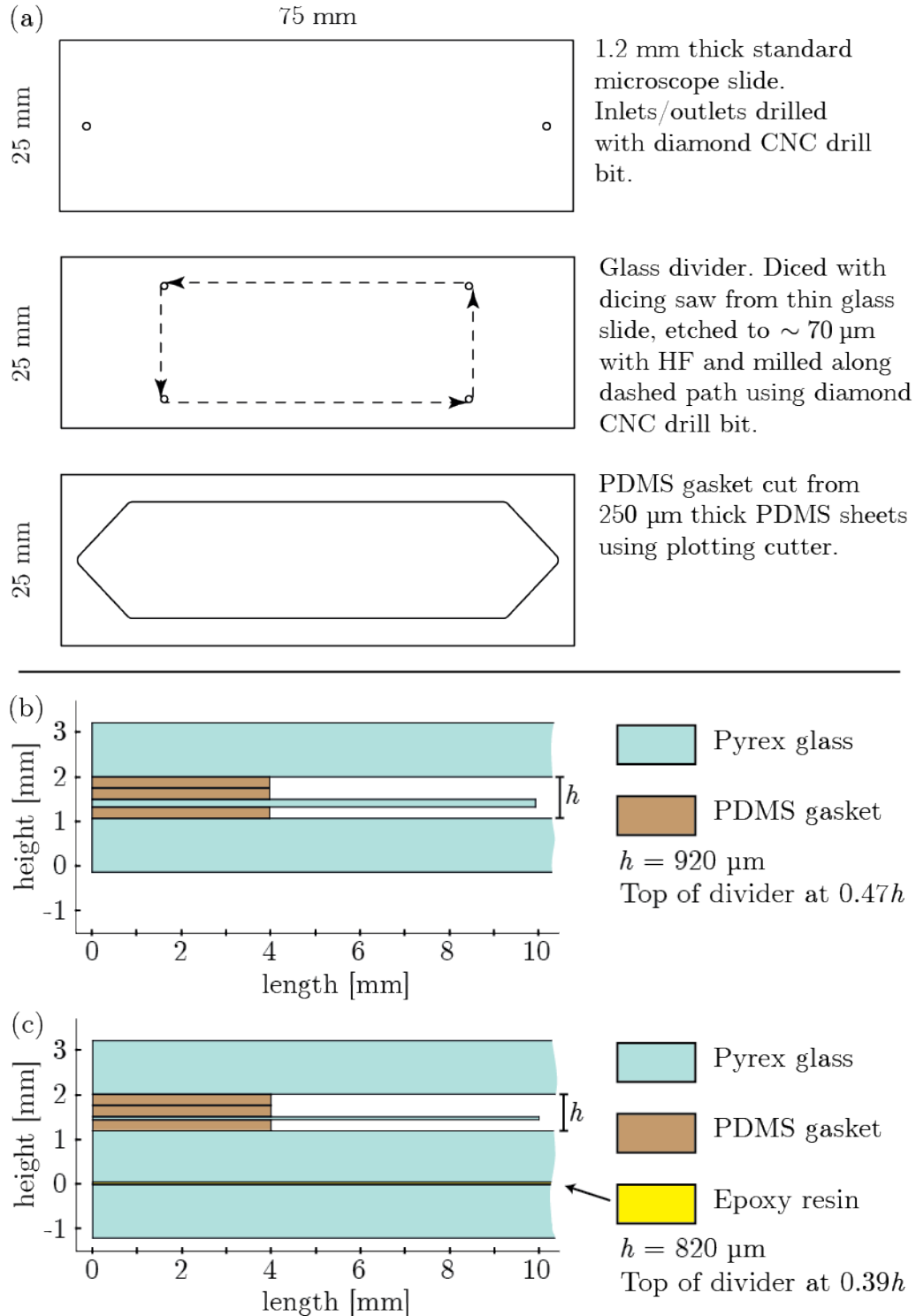
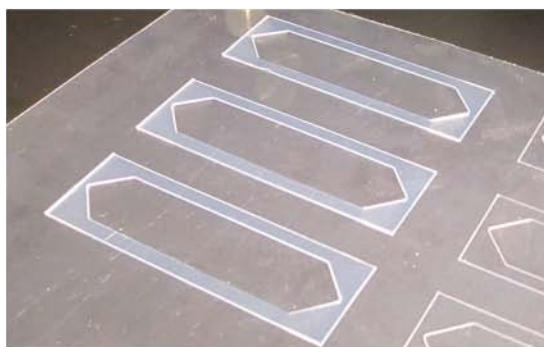


Figure 3.3: (a) Top-view of device layers. (Top to bottom): Thick glass reflectors with inlet/outlet holes, thin glass flow-divider and PDMS gasket showing  $17 \text{ mm} \times 55 \text{ mm}$  separation channel. (b)-(c) Cross-sectional view of the layered assembly of first-generation device (b) and second-generation device (c). Glass/PDMS layers are plasma bonded and the two cover glass pieces in the second-generation design are bonded with a thin ( $\sim 50 - 100 \mu\text{m}$ ) layer of epoxy resin. The channel height,  $h$ , was  $920 \mu\text{m}$  and  $820 \mu\text{m}$  for the first- and second-generation device, respectively.



(a) Machined glass divider and cover glass.



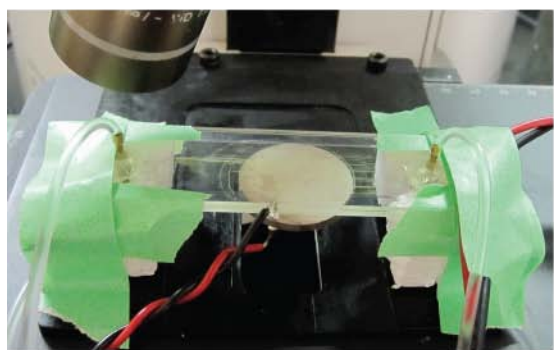
(b) PDMS gaskets.



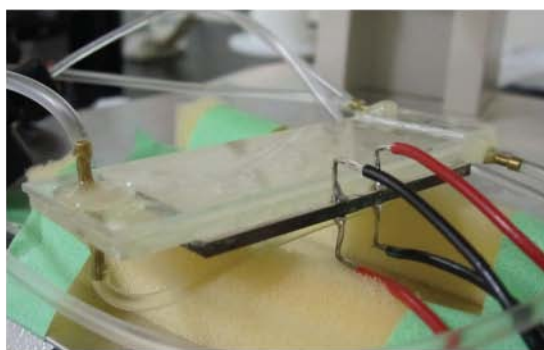
(c) Plasma bonding device layers.



(d) Final glass/PDMS channel with brass in/outlets set in epoxy resin.



(e) 1st generation design. Symmetric glass reflectors. Actuation with round piezo set in ultrasound gel.



(f) 2nd generation design. Asymmetric glass reflectors. Actuation with piezo under full channel set in epoxy resin.

Figure 3.4: (a)-(d) Outline of device assembly. (e)-(f) Fully assembled devices with piezo actuators and inlet and outlet tubing.

generation design; Additional small PDMS gaskets and a thin glass piece was plasma bonded at the outlets to allow us to easily see the fraction of particles going out each outlet, see Fig. 3.5.

The first-generation design was actuated with a single round, 4 cm-diameter Ferroperm

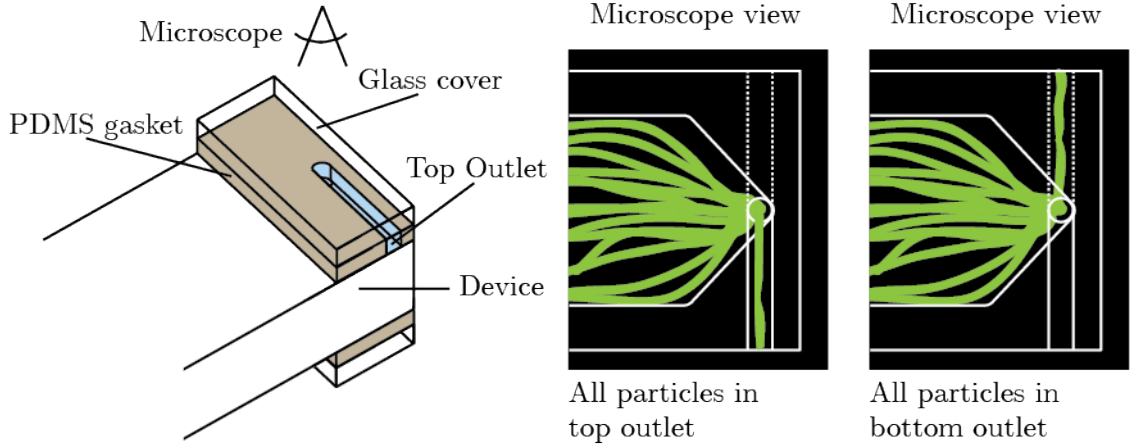


Figure 3.5: (left) Second-generation design of outlets. An additional PDMS gasket and thin cover glass was plasma bonded at the outlets in the second-generation device to make a horizontal outlet channel at the top and bottom outlets. The two outlet channels went to opposite sides of the device. This made it possible to see with a microscope, if the beads were exiting the device via the bottom or top outlet. To minimize shear forces in the outlet channel to allow for application of the device to separation of biological cells, the fluidic resistance of the channel was reduced by bonding three identical 250  $\mu\text{m}$  PMDS gaskets, giving outlet channel cross-section dimensions width  $\times$  height = 1.1 mm  $\times$  750  $\mu\text{m}$ . (right) Microscope view showing green fluorescent particles exiting the device via the bottom and top outlets.

Pz26-actuator with a resonant frequency of 1 MHz attached beneath the microchannel with cyanoacrylate superglue. The second-generation design was actuated with two 27 mm  $\times$  27 mm with a resonant frequency of 1 MHz diced from circular Ferroperm Pz26-actuators and set in cyanoacrylate superglue so they cover the full separation microchannel.

### 3.2.3 External setup

The piezo actuators were driven with a digital function generator amplified with a floating op-amp capable of driving the piezo actuators with a MHz-frequency sine waveform at  $\sim 60 V_{\text{pp}}$  with no appreciable signal distortion. The device was mounted in a stable fluidic setup with 500  $\mu\text{m}$  teflon tubing and buffer and sample flows were injected with dual programmable syringe pumps at a flowrate ratio,  $Q_{\text{buffer}}/Q_{\text{sample}} = 3$ . The outlet tubing of the device was matched to the internal fluidic resistance of the device, so that the outlet flow ratio was  $Q_{\text{top}}/Q_{\text{bot}} \approx 2.1$ , more on this in Section 3.4.2. The temperature of the device was continuously measured using a chromel/alumel thermocouple, see Fig. 3.1(b). To maintain a constant device temperature, the device was mounted in thermal grease on an custom-machined aluminium heatsink, see Fig. 3.1. The aluminium heatsink was mounted in thermal grease on a Peltier element driven with a variable DC power source to control the heat sink temperature. The Peltier element was mounted in thermal grease on another aluminium heat sink cooled with an air fan.

### 3.3 Theoretical estimate of resonant frequency

#### 3.3.1 Validity of 1D-model

When the chip is on resonance, the piezo actuation induces standing half-wavelength resonant plane wave modes in the rectangular water channel in all three orthogonal dimensions: length, width and height. For the purpose of our acoustophoretic separation, we want to establish modes, where we have a half-wave pressure mode in the height dimension with a pressure node in the middle of the channel. We want to estimate the resonance frequency theoretically, so we can find an experimentally working frequency. To fully calculate the resonances in the chip, we would have to make a full 3D model of the chip and piezo geometry and couple the pressure waves in the fluids, the elastic waves in the glass/PDMS structure and the sinusoidally varying piezoelectric response amplitude, but this is beyond the scope of this particular project.

We expect from Eq. (2.45), that the resonant frequency increases, the more waves are standing along the length and width of the channel. Due to the orthogonality of length, width and height, we can rewrite the acoustic Helmholtz wave equation, Eq. (2.42) for pressure as,

$$\underbrace{(-k_x^2 - k_y^2)}_{-k_0^2} p + \partial_z^2 p = -\frac{\omega^2}{c_a^2} p, \quad (3.1)$$

where we introduce  $k_0^2 = k_x^2 + k_y^2$ , so  $k = k_0 + k_z$  and a coordinate system as in Fig. 3.6. From Eq. (2.45) we see that for our channel where the height is by far the smallest length scale, the resonance frequency will be determined by the waves in this dimension, as the large aspect ratio ensures us  $k_0 \ll k$ . We can let  $k_0$  take some finite value as a way to model the contribution to the full wave vector  $\mathbf{k}$  from the resonant modes in the  $y$ - and  $z$ -dimensions and consider only a 1D model of the resonances to get an estimate of the right piezo actuation frequency. In Fig. 3.6(a)-(f) we show, how very close the frequencies of various resonances are to the simple 1D wave (Fig. 3.6(a)). At resonance, we could actually see the axial resonances experimentally as formation of distinct bands of particles in the  $xy$ -plane, see Fig. 3.6, bottom. Actually, this is a novel feature of our design; When sweeping the frequency to find a good resonant frequency, it is possible to determine the strength of the pressure mode by observing the formation of the axial bands.

#### 3.3.2 Calculation of resonant frequency

Concerning ourselves with the small height dimension only, we can calculate the resonant frequencies of the microfluidic chip using wave-transfer mechanics. Consider the water channel as a 1D glass/water/glass-sandwich, see Fig. 3.7. We introduce We call the pressure fields in the three domains,

$$p = p_1(z), \quad \text{for } 0 < z < a \quad (3.2)$$

$$p = p_2(z), \quad \text{for } a < z < b \quad (3.3)$$

$$p = p_3(z), \quad \text{for } b < z < h \quad (3.4)$$

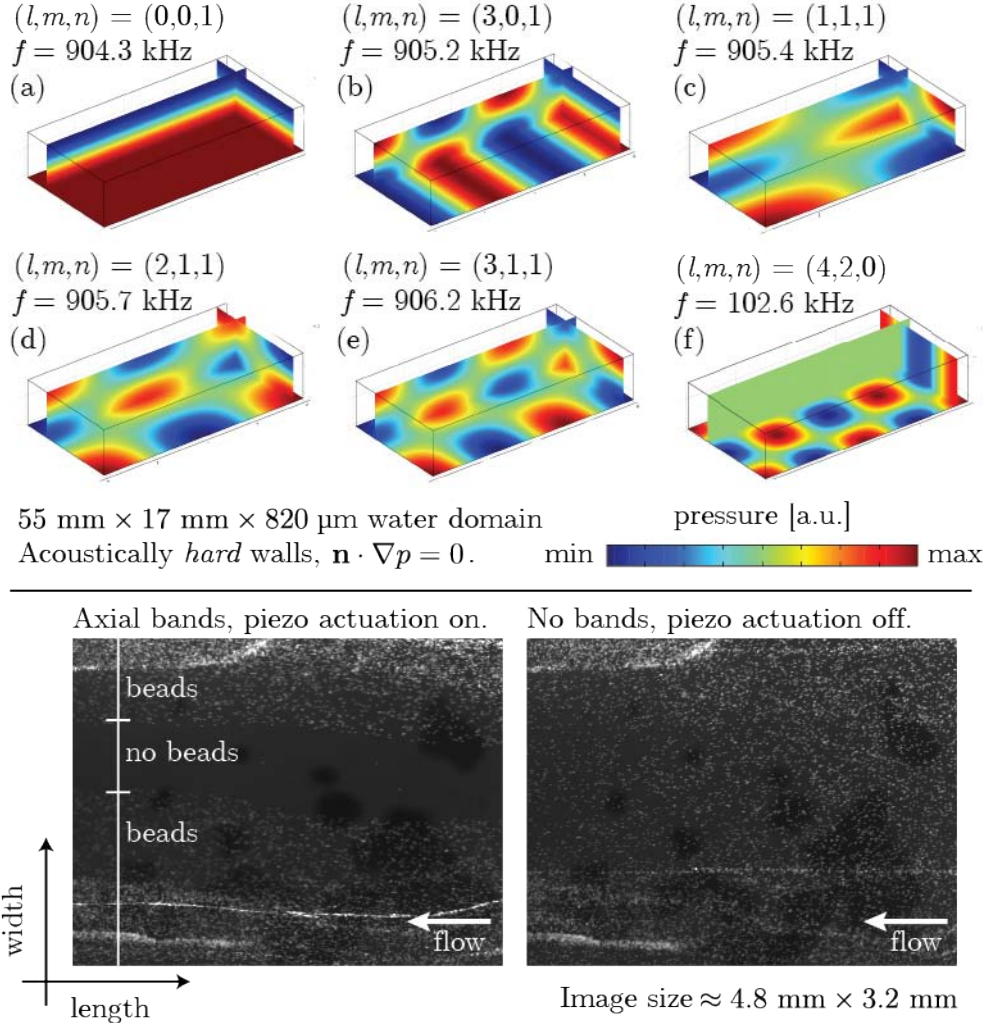


Figure 3.6: **Top** (a)-(f) Resonant frequencies and pressure fields for resonant modes in a 55 mm  $\times$  17 mm  $\times$  820  $\mu$ m water box with acoustically *hard* walls. Due to the large aspect ratio of the channel, the resonant frequencies with a half-wave in the height (a)-(e) lie very close to the pure 1D resonance (a) in frequency space, while resonances with no half-wave in the height lie far away in frequency space, for instance (f). **Bottom** Experimentally observed bands of particles due to axial pressure modes when on resonance (left) compared to no bands without piezo actuation (left). Image size approximately 4.8 mm  $\times$  3.2 mm.

and introduce the ratios  $\alpha = c_{py}/c_{wa}$  and  $\beta = \rho_{py}/\rho_{wa}$  between the water and glass densities and speeds of sound, respectively. At the piezo actuator (far left), we have maximum pressure and at the air interface (far right), we require, that the pressure is equal to the surrounding atmospheric pressure. At the glass/water interfaces, we require continuity as in Eq. (2.55) and Eq. (2.56). This gives us the following boundary conditions

on the pressure field,  $p(z)$ :

$$\partial_z p_1(0) = 0, \quad (\text{max } p \text{ at piezo}) \quad (3.5a)$$

$$p_1(a) = p_2(a), \quad (\text{continuity}) \quad (3.5b)$$

$$\partial_1 p_1(a) = \beta \partial_z p_2(a), \quad (\text{continuity}) \quad (3.5c)$$

$$p_2(b) = p_3(b), \quad (\text{continuity}) \quad (3.5d)$$

$$\beta \partial_1 p_2(b) = \partial_z p_3(b), \quad (\text{continuity}) \quad (3.5e)$$

$$p_3(H) = 0. \quad (p = 0 \text{ at air}) \quad (3.5f)$$

To satisfy Eq. (3.5a), we can exclude a sine wave in domain (1), so we guess solutions to the wave equation,

$$p_1 = \cos(k_{\text{py}}z), \quad (3.6)$$

$$p_2 = A \sin(k_{\text{wa}}z) + B \cos(k_{\text{wa}}z), \quad (3.7)$$

$$p_3 = C \sin(k_{\text{py}}(z - h)) + D \cos(k_{\text{py}}(z - h)). \quad (3.8)$$

where we have scaled the pressure amplitudes, so the pressure is 1 at the piezo actuator ( $z = 0$ ) and introduce the amplitudes,  $A$ ,  $B$ ,  $C$  and  $D$ , to be determined. From the wave equation, Eq. (3.1), we get,

$$\partial_z^2 p_1 = - \underbrace{\left[ \frac{\omega^2}{\alpha^2 c_{\text{wa}}^2} - k_0 \right]}_{k_{\text{py}}^2} p_1, \quad \partial_z^2 p_2 = - \underbrace{\left[ \frac{\omega^2}{c_{\text{wa}}^2} - k_0^2 \right]}_{k_{\text{wa}}^2} p_2, \quad \partial_z^2 p_3 = - \underbrace{\left[ \frac{\omega^2}{\alpha^2 c_{\text{wa}}^2} - k_0^2 \right]}_{k_{\text{py}}^2} p_3. \quad (3.9)$$

Writing down the transfer-matrices at the glass/water interfaces yields,

$$\begin{bmatrix} \cos(k_{\text{py}}a) \\ -k_{\text{py}} \sin(k_{\text{py}}a) \end{bmatrix} = \begin{bmatrix} \sin(k_{\text{wa}}a) & \cos(k_{\text{wa}}a) \\ \beta k_{\text{wa}} \cos(k_{\text{wa}}a) & -\beta k_{\text{wa}} \sin(k_{\text{wa}}a) \end{bmatrix} \begin{bmatrix} A \\ B \end{bmatrix} \quad (3.10)$$

$$\begin{aligned} & \begin{bmatrix} \sin(k_{\text{wa}}b) & \cos(k_{\text{wa}}b) \\ \beta k_{\text{wa}} \cos(k_{\text{wa}}b) & -\beta k_{\text{wa}} \sin(k_{\text{wa}}b) \end{bmatrix} \begin{bmatrix} A \\ B \end{bmatrix} \\ & = \begin{bmatrix} \sin(k_{\text{py}}(b - h)) & \cos(k_{\text{py}}(b - h)) \\ k_{\text{py}} \cos(k_{\text{py}}(b - h)) & -k_{\text{py}} \sin(k_{\text{py}}(b - h)) \end{bmatrix} \begin{bmatrix} C \\ D \end{bmatrix} \quad (3.11) \end{aligned}$$

Combining Eq. (3.10) and Eq. (3.11) to eliminate  $(A, B)$  yields  $(C, D)$  in terms of  $k_{\text{wa}}$  and  $k_{\text{py}}$ , and thus as a function of  $\omega$ . For Eq. (3.8) to satisfy Eq. (3.5f) we must require that  $D = 0$ . By solving this system of equations numerically using MATLAB, we can find frequencies  $f = 2\pi\omega$ , so  $D = 0$  i.e. satisfying the boundary conditions on the pressure field.

In Fig. 3.8, we show resonant frequencies calculated for  $k_0 = 0$  (i.e. no axial modes, as in Fig. 3.6(a)) for the first-generation and second-generation device. We see, that the

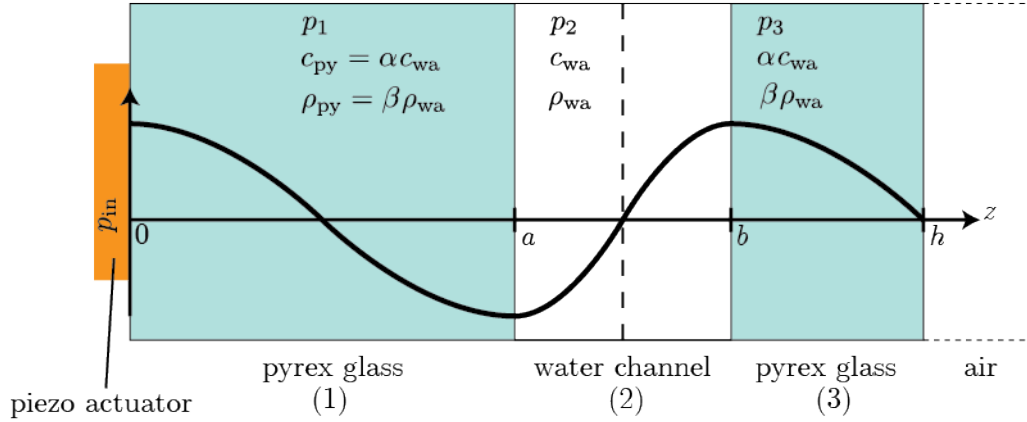


Figure 3.7: 1D approximation for calculation of resonant frequency showing how the asymmetric glass reflectors in the second-generation device are designed to support a half-wave in pyrex domain (1), a half-wave in the water domain (2) and a quarter-wave in the pyrex domain (3) to ensure a strong resonance.

asymmetric glass reflector setup in the second-generation device allows for much stronger resonances with a strong half-wave resonance at  $f = 925$  kHz, see Fig. 3.8(d). This is due to the fact, that we have in fact designed the device geometry to support the resonance. The ratio of wavelengths in glass and water at a given frequency is given by  $\lambda_{py}/\lambda_{wa} = c_{py}/c_{wa} \approx 3.8$ , using values from Table 2.2. The ratio between a half-channel height,  $1/2h$ , and the glass reflector thickness,  $t$ , is  $2t/h \approx 2.9$ , meaning that we are very close to being able to maintain full pressure amplitude across the channel in the 1D propagating wave approximation. This is one of the main strongpoints of the second-generation design and something, that has not been considered in the literature before.

## 3.4 Device plumbing

### 3.4.1 Flow and shear stress

A more thorough investigation of the device fluidics was necessary for several reasons. Firstly, it was important for the design of the device tubing setup to have control of the outlet flow ratio. Secondly, since we want to eventually use the device to separate biological cells, we have to design the fluidics, so the shear forces are not harmful to the cell viability. Using the device at a total flowrate in the order of liters per minute gives a typical velocity  $V_0 = Q_{total}/\mathcal{A}$ , where  $\mathcal{A} = hw$  is the cross-sectional area. A typical length-scale of the flow,  $L_0$  is the channel height  $h$ . This gives a Reynolds number for the flow,

$$Re = \frac{\rho V_0 L_0}{\eta} \approx 16, \quad (3.12)$$

where we have used  $Q_{total} \sim 1$  L/h and values from the second-generation design. This Reynolds number is low enough for us to assume laminar flow in the channel. This

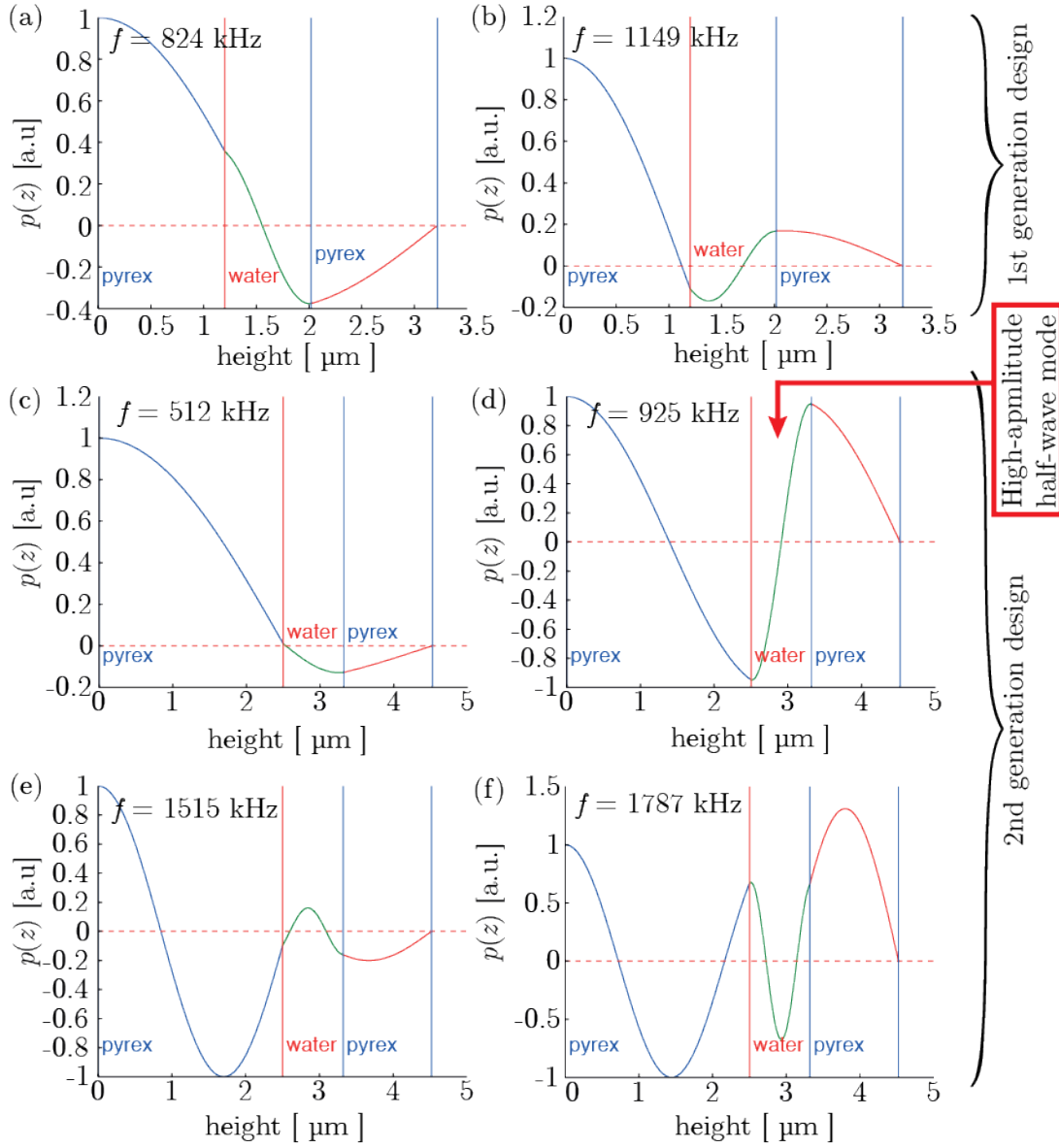


Figure 3.8: Resonance frequencies for first-generation device (a)-(b) and second-generation device (c)-(f), showing how the asymmetric glass reflectors allow for a much stronger half-wave resonance in the second-generation device at 925 kHz (d), than is possible in the first-generation device (a)-(b). These considerations regarding matching of device geometry to wavelengths has not been reported in the literature before, but we show that by matching the channel and reflector widths to the ratio between speeds of sound and by using asymmetric reflectors, the resonance properties of the device can be improved significantly.

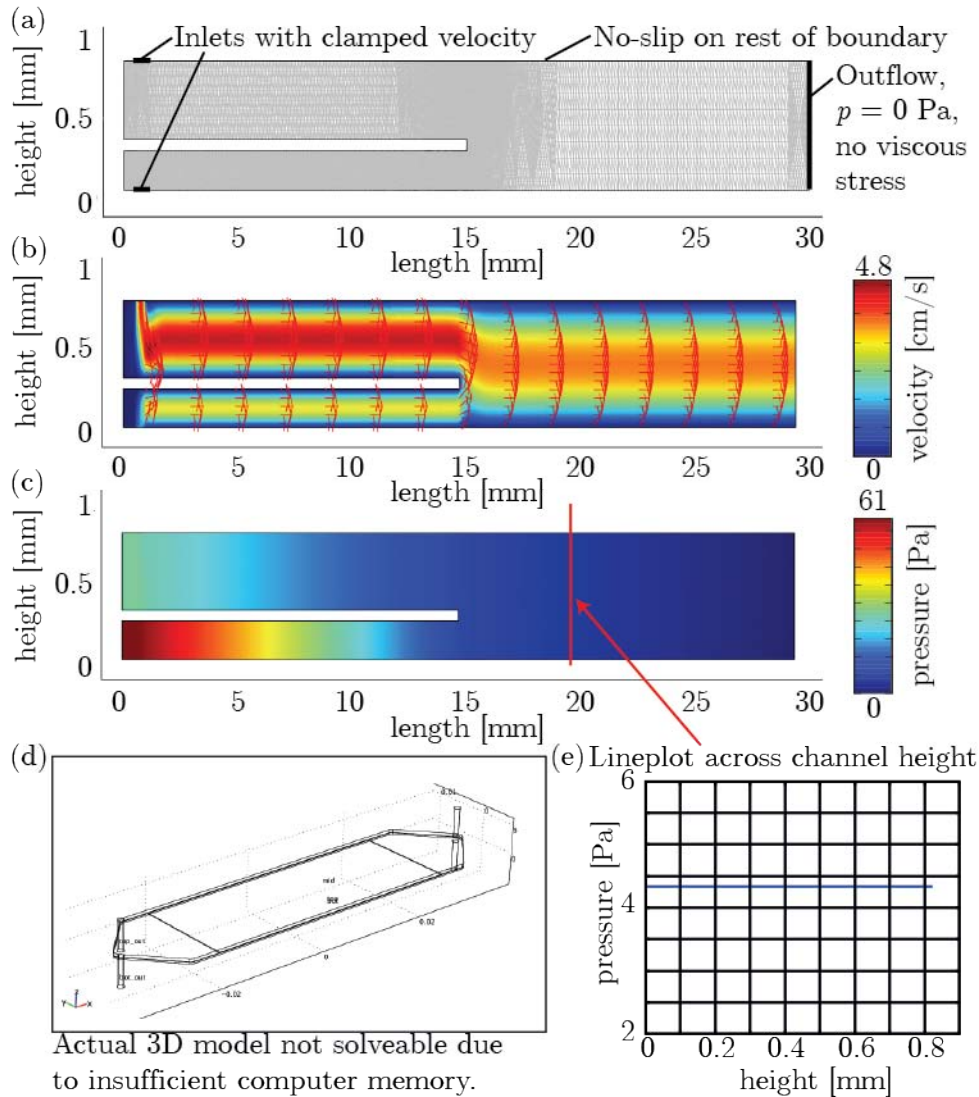


Figure 3.9: Finite element method calculations of flow in device at 1 L/h total throughput. (a) Schematic of the simplified 2D model solved in COMSOL showing sufficient mesh found with convergence analysis. (b) Color plot of the magnitude of the velocity field with red arrows showing the direction of the velocity vector. The flow profile is very close to the parabolic flow profile expected from laminar Poiseuille flow and the flow develops smoothly and passes over the glass divider without turbulent effects mixing the fluid layers. The velocity gradients give shear rates on physiological orders of magnitude. (c) Color plot of the pressure field showing that the pressure is uniform across the device height due to laminarity and that the pressure is largest near the bottom inlet as is expected from the larger hydraulic resistance of the smaller bottom inlet. (d) The full 3D model was not solvable, even if cut along symmetry planes. (f) Plot of the pressure along the device height validating that due to laminarity, the pressure across the height of the whole channel becomes equal.

was verified with a finite element model in COMSOL, see Fig. 3.9. An actual 3D model of the device was made, but it was not possible to mesh and solve this model due to insufficient computer memory, so instead, a simplified 2D model was investigated. In the bulk water domain, the incompressible Navier-Stokes equation, Eq. (2.5) was solved under the following boundary conditions: (i) Parabolic Poiseuille flow velocity profiles, Eq. (2.9), yielding 0.75 L/h and 0.25 L/h inflow at 1.1 mm top and bottom inlets, respectively. (ii) Laminar outflow into bulk channel by clamping  $p = 0$  at far right, and imposing no viscous stress. (iii) No-slip ( $\mathbf{v} = 0$ ) at all other boundaries. As shown in Fig. 3.9, we see that the flow in the channel is indeed laminar and that the pressure across the channel height is completely uniform immediately after the glass divider. We also see, that the maximum shear rate,  $\dot{\gamma} = |\nabla \mathbf{v}|$  in the channel is on the order  $\dot{\gamma} \sim 100 \text{ s}^{-1}$ , leading to shear stress,  $\tau_{\text{shear}}$ , on the order of

$$\tau_{\text{shear}} = \dot{\gamma}\eta \approx 0.1 \text{ Pa.} \quad (3.13)$$

The highest shear stress must be in the the 500  $\mu\text{m}$  teflon inlet and outlet tubing, as this tubing has the smallest cross-sectional area. The shear rate for a cylindrical tube can be calculated from the parabolic Poiseuille flow velocity profile,

$$\dot{\gamma} = \partial_r v(r) = \partial_r \left[ \frac{\Delta p}{4 \eta L} (a^2 - r^2) \right] = \frac{4Q_{\text{total}} r}{\pi a^4}. \quad (3.14)$$

The shear stress will be largest at the channel walls, where  $r = a$ , which gives  $\tau_{\text{shear}} \approx 22 \text{ Pa}$ . This is quite a high shear force compared to physiological shear rates, which are typically on the order of 1 Pa[28]. However, cells can generally tolerate quite high constant shear rates, but are much more sensitive to shear rate gradients [21], meaning that it might turn out be necessary to try to get a uniform cross-section in all the external device fluidics to maintain constant shear rates and good cell viability for biological applications of the device.

### 3.4.2 External tubing

From Fig. 3.9, we see that due to laminarity, the pressure will be uniform across the channel height<sup>3</sup> immediately before the glass divider and we know, that at the outlet openings the pressure will equal to the atmospheric pressure. Using this, we could treat the top outlet fluidics and the bottom outlet fluidics as two hydraulic resistors connected in parallel and use the Hagen-Poiseuille law, Eq. (2.29), to calculate the appropriate lengths of the outlet tubing from the device to ensure the correct outlet flowrate ratio, see Fig. 3.10(a)-Fig. 3.10(b).

The ratio between the cross-sectional areas of the channel going below the divider and above the divider at the outlets is 1:2. However, because the fluidic resistance scales inversely with the smallest length-scales to a power of four, the resistance ratios will not be 1:2 and there will be a much larger proportion of the flow out the top outlet than the bottom outlet. Furthermore, in microfluidics it is usually the case that the internal fluidic resistance of the device is much larger than the resistance of the external tubing and thus

---

<sup>3</sup>where we neglect the hydrostatic pressure as usual.

completely dominates. However, in our case, the external 500  $\mu\text{m}$  teflon tubing actually has a much higher resistance than the device and thus is actually determining the outlet flow ratios. Using the verification of laminarity from Fig. 3.9, we could calculate the right length of the outlet tubing by calculating the fluidic resistance of every fluidic component (e.g. tubes, valves, connectors) and the device (approximating it with piecewise constant components: cylindrical domains, rectangular domains, triangular domains etc. in series), see Fig. 3.11. The simple but tedious calculations were done in MATLAB, and the tubing was mounted, so the estimated ratio between the hydraulic resistances was  $R_{\text{bot}}/R_{\text{top}} = 3$ , see Fig. 3.11. The ratio between the internal device resistance and the resistance of the external tubing was 1.11 and 3.22 for the top and bottom outlets, respectively, showing that the resistance is indeed determined by the external tubing. This is actually a very nice feature, and has not previously been considered in the literature; By changing the external tubing, the flowrate ratio inside the device at the glass divider can be easily manipulated, adding a novel degree of freedom to the device design, that might be handy when optimizing the experimental setup for good acoustophoretic separation.

From actual measurements, we find the flowrate ratio to depend approximately linearly on temperature and voltage as shown in Fig. 3.10(c) and Fig. 3.10(d). From linear fits with MATLAB, we find

$$\frac{Q_{\text{top}}}{Q_{\text{bot}}}(T) = 2.13 + 3.91 \times 10^{-4} \text{ K}^{-1} \cdot (T - 273 \text{ K}) \quad \text{norm(res)} = 0.726 \quad (3.15)$$

$$\frac{Q_{\text{top}}}{Q_{\text{bot}}}(Q_{\text{total}}) = 2.20 + 0.203 \frac{\text{h}}{\text{L}} \cdot Q_{\text{total}} \quad \text{norm(res)} = 0.595 \quad (3.16)$$

To a very good approximation, the flowrate ratio does not change with a temperature increase. This is no surprise, as it is known from perturbation calculations that the temperature dependence of viscosity only leads to a very minute change of the regular isothermal Poiseuille flow velocity profiles[5]. The flowrate ratio is more dependent on total flowrate, which is expected since the increase in flowrate leads to an increase in fluid velocity and thus a larger Reynolds number. For increasing Reynolds numbers, the Hagen–Poiseuille law becomes less and less valid and thus we expect some deviation. The flowrate ratios were measured by simultaneously collecting  $\sim 1.5$  mL samples in microcentrifuge tubes from the top and bottom outlets for some time. The uncertainty on the measurements corresponds to one drop of sample, see Fig. 3.12. Using theory of error propagation, the errorbars plotted in Fig. 3.11 were calculated by assuming the mass of a drop of sample to be 50 mg.

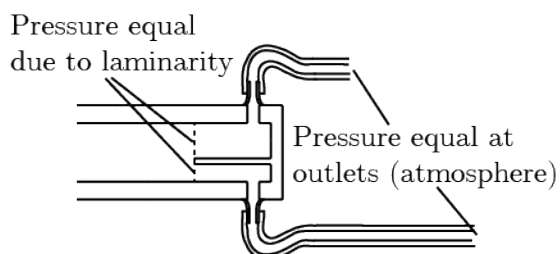
### 3.5 Main separation results

The main separation results of this thesis is shown in Fig. 3.13(c). We show very good separation of 3  $\mu\text{m}$  red fluorescent and 10  $\mu\text{m}$  green fluorescent polystyrene beads at 1 L/h total throughput, 15 V<sub>pp</sub> piezoactuation at  $f_{\text{center}} = 899 \text{ kHz}$ <sup>4</sup>. This throughput is approximately one hundred times higher than previously reported in the literature

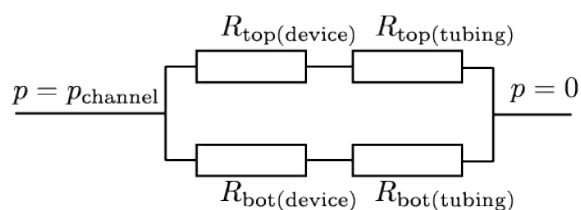
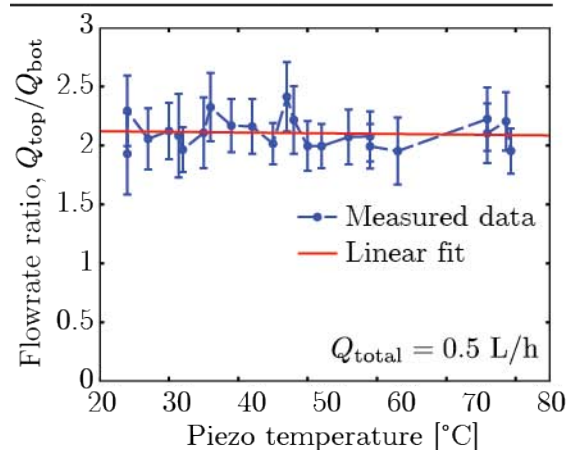
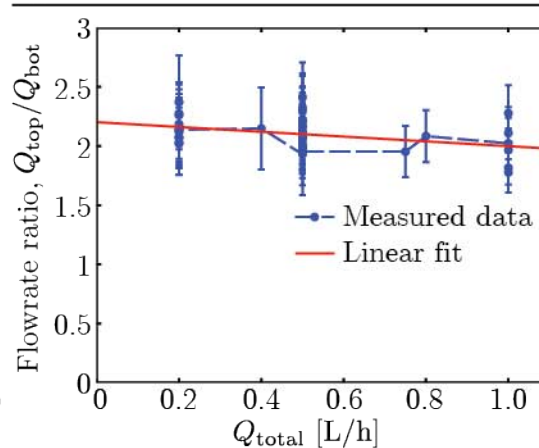
---

<sup>4</sup>The theoretical estimate yielded  $f = 925 \text{ kHz}$ , see Fig. 3.8.

(a) Device schematic



(b) Equivalent circuit model

(c) Flowrate ratio dependence on  $T$ (d) Flowrate ratio dependence on  $Q$ 

(e) Device mounted with tubing and valves

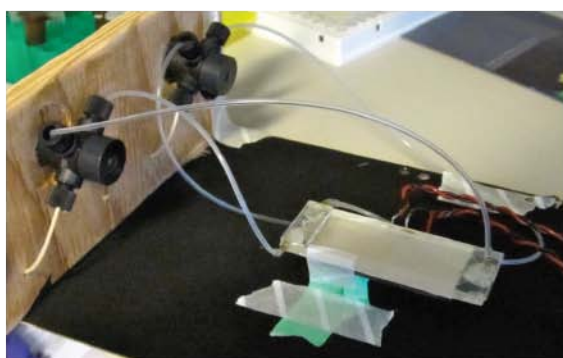
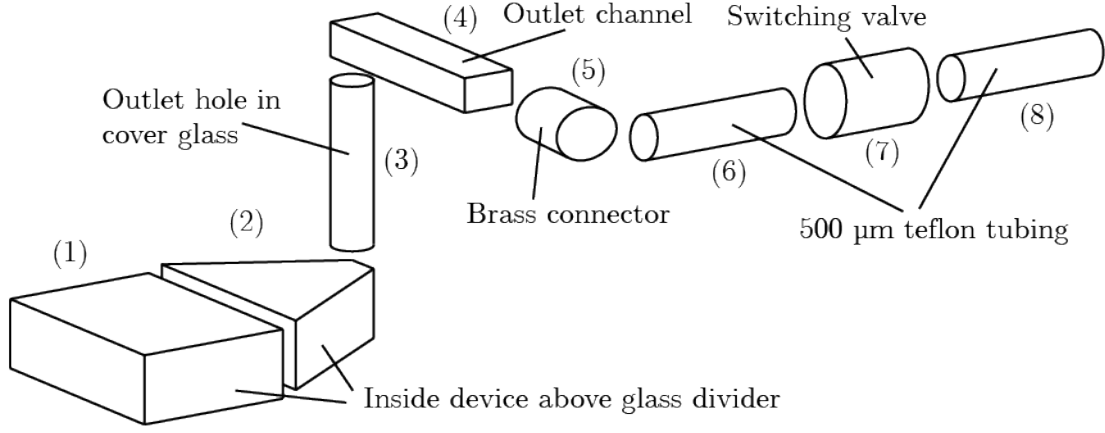


Figure 3.10: Device plumbing. (a) Sketch of the actual device. (b) Equivalent fluidic circuit. (c) Experimental data showing that the outlet flow ratio is approximately constant over a wide temperature range, so we can neglect affects from the slight temperature dependence of viscosity. (d) Experimental data showing that the outlet flow ratio changes slightly with increasing flowrate due to increasing Reynolds number. (e) Picture of actual fluidic setup with teflon tubing of lengths matching the internal device resistance and switching valves to close off the device flow to avoid air bubbles.



Approximation		Expression for $R_{\text{hyd}}$	$R_{\text{hyd}}$ Pa s/m <sup>3</sup>
(1)	Rectangular	$\frac{12 \eta L}{1 - 0.63(h/w)} \frac{1}{h^3 w}$	$2.88 \times 10^8$
(2)	Trapezoid	$\int_0^L \frac{12 \eta}{1 - 0.63(h/w(L'))} \frac{1}{h^3 w(L')} dL'$	$2.18 \times 10^7$
(3)	Cylindrical	$\frac{8}{\pi} \eta L \frac{1}{a^4}$	$3.34 \times 10^7$
(4)	Rectangular	$\frac{12 \eta L}{1 - 0.63(h/w)} \frac{1}{h^3 w}$	$5.92 \times 10^8$
(5)	Cylindrical	$\frac{8}{\pi} \eta L \frac{1}{a^4}$	$1.67 \times 10^8$
(6)	Cylindrical	$\frac{8}{\pi} \eta L \frac{1}{a^4}$	$4.59 \times 10^9$
(7)	Cylindrical	$\frac{8}{\pi} \eta L \frac{1}{a^4}$	$3.82 \times 10^7$
(8)	Cylindrical	$\frac{8}{\pi} \eta L \frac{1}{a^4}$	$3.05 \times 10^9$

Figure 3.11: (Top) Sketch of the calculation of the total outlet resistance of the top outlet using equivalent circuit theory. The many stages of the device and the external fluidics are approximated by fluidic resistors in series. (Bottom) Table showing the calculated fluidic resistance of each part of the top outlet resistance demonstrating that the total fluidic resistance is dominated by the resistance of the 500  $\mu\text{m}$  teflon tubing. The ratio between the internal device resistance and the resistance of the external tubing was 1.11 and 3.22 for the top and bottom outlets, respectively.

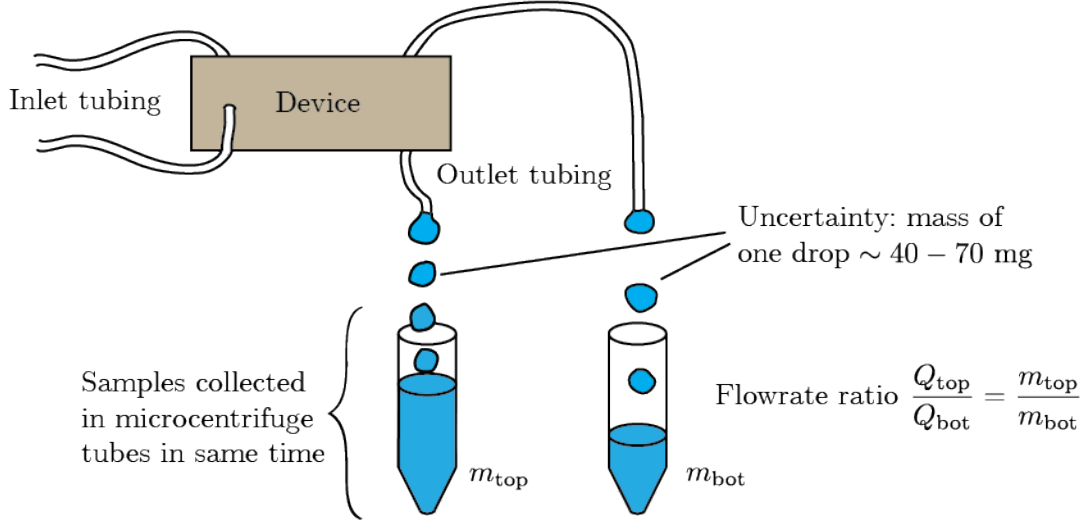


Figure 3.12: Sketch of experimental collection of samples from the top and bottom outlets showing that the uncertainty on the measured flowrate ratio is determined by the mass of one drop of sample.

[14, 16]. We see that sweeping  $f_{\text{center}} \pm 10$  kHz at 1 ms modulation period increases separation efficiency, more on this in Section 3.6. The data has been corrected for a small background of beads stuck in the device fluidics, measured by running the device with buffer in both inlets. The bead densities in the outlet fractions were analyzed using flow cytometry, and the flowrates were measured by weighing samples collected in centrifuge tubes. Using the Peltier element, the device temperature was kept constant throughout the experiment. Notice, that the resonance frequency is in good agreement with the 1D approximation, see Fig. 3.8. The transfer rate,  $t$ , was defined as the fraction of beads going out the top outlet,

$$t = \frac{\rho_{\text{top}}}{\rho_{\text{top}} + \rho_{\text{bot}} \frac{Q_{\text{bot}}}{Q_{\text{top}}}}, \quad (3.17)$$

where  $\rho_{\text{top(bot)}}$  and  $Q_{\text{top(bot)}}$  are the counted densities and volumetric flowrates of the top(bottom) outlet respectively.

The microcentrifuge tubes are shaken with a micromixer before FACS analysis to ensure uniform bead distribution and the actual counting numbers are several thousand beads, giving a neglectable  $\sqrt{N}$ -uncertainty on the bead densities. This means, that the uncertainty on  $t$  stems from the uncertainty on the flowrate ratio. Since temperature and inlet flow is kept constant for a separation experiment, we know that the flowrate is constant. The flowrate ratio used to calculate the transfer was found by collecting samples of inlet and outlet fractions in regular centrifuge tubes in triplicates. We found, that the flowrate ratio was indeed very constant, and the large sample size made the uncertainty due to one drop of sample neglectable. In this thesis, we shall plot the transfer rates without error-bars because they all just based on one point. The relevant errors do not stem from propagation of measurement uncertainty, but rather from statistical errors due

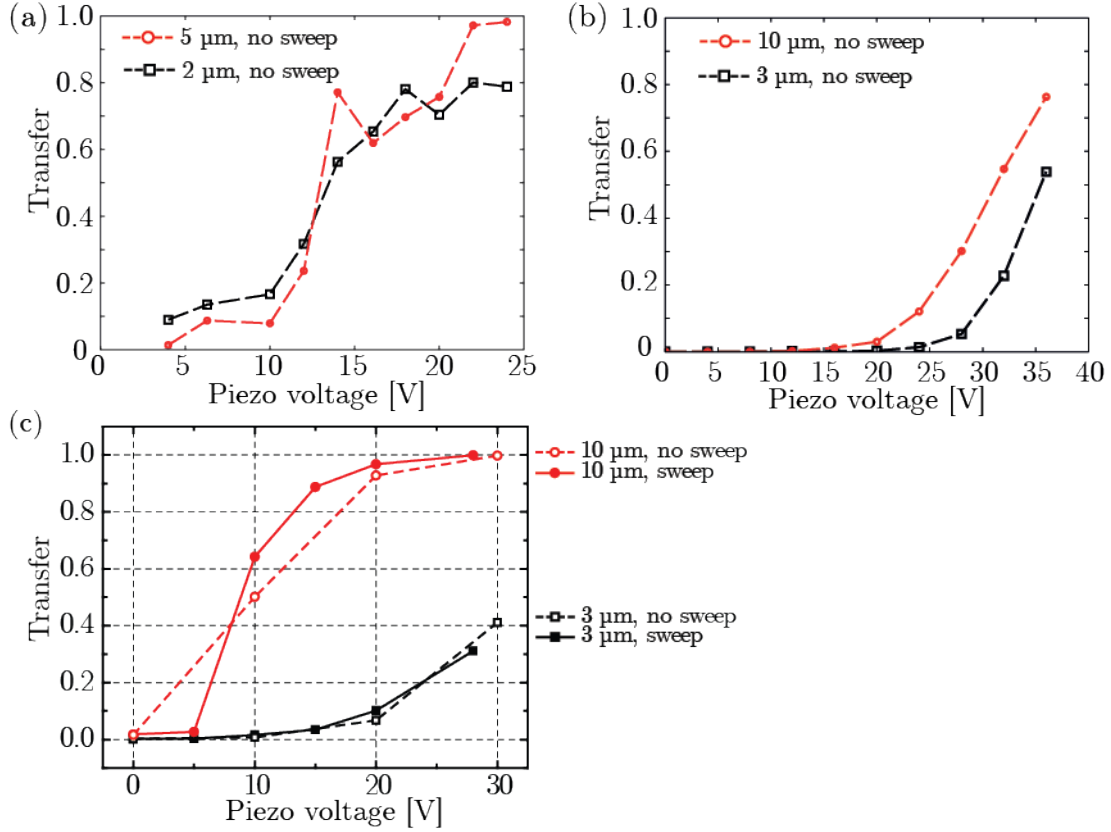


Figure 3.13: (a) Preliminary separation results for 2  $\mu\text{m}$  and 5  $\mu\text{m}$  polystyrene beads at 0.5 L/h and  $f_{\text{center}} = 1026$  kHz. This data was recorded before temperature control was implemented, and the temperature increased from 24°C to 45°C from low to high voltage. Confer Fig. 3.14(b), we expect to be able to achieve better separation with the temperature controlled setup. (b) Similar preliminary separation results for 3  $\mu\text{m}$  and 10  $\mu\text{m}$  polystyrene beads at 1 L/h and  $f_{\text{center}} = 1026$  kHz with  $\pm 10$  kHz linear sweep with a preliminary temperature control setup allowing for temperature control within a few °C. (c) The best particle separation of 3  $\mu\text{m}$  and 10  $\mu\text{m}$  polystyrene beads achieved before the deadline of this thesis: Fraction of beads in the top outlet (transfer) at 1 L/h throughput showing strong separation at 15 V<sub>pp</sub> and  $f_{\text{center}} = 899$  kHz. Sweeping around  $f_{\text{center}}$  in a  $\pm 10$  kHz window with a 1 ms modulation period increases separation efficiency. The data in (a)-(c) has been corrected for a small background, measured by running the device with buffer in both inlets. For uncertainties, refer to Sec. 3.5.

to reproducibility of measurements. The separation data graphs in this thesis are not of proper publication quality as each point would have to be done in at least triplicates to get an estimate of the reproducibility. This will be done properly, when we collect the data for actual publication of the fully optimized device<sup>5</sup>. The graphs presented here do however show the relevant trends for the preliminary results. Also, it is worth to point out to the reader, that collecting samples for L/h throughput data points with 50 mL-capacity syringe pumps is a very lengthy and tedious affair, and that the FACS analysis of the inlet and outlet fractions amounts to several minutes pr. datapoint.

We see, that if the piezo actuation is turned off, there is no transfer of beads to the top outlet. We know from Fig. 3.9 that the device flow is completely laminar with characteristic velocities on the order of cm/s. By estimating the diffusion constant for the 3  $\mu\text{m}$  beads by the Einstein diffusion constant, Eq. (2.12), and taking the device height as a characteristic length scale, we find the Péclet number for the beads,  $Pe = 7 \times 10^9$ , ensuring no diffusion of beads across the channel height.

Fig. 3.13(a) shows results from similar experiments done with 2  $\mu\text{m}$  red fluorescent and 5  $\mu\text{m}$  green fluorescent polystyrene beads at 0.5 L/h total throughput. We were not able to optimize the experiment to get good separation for these sizes before the deadline of this thesis. However, Fig. 3.13(a) is a very promising preliminary result. Fig. 3.13(b) shows similar preliminary data for separation of 3  $\mu\text{m}$  and 10  $\mu\text{m}$  beads, leading us to believe, that by careful optimizing of the experimental setup (temperature control, fluidics, piezo frequency), separation of 2  $\mu\text{m}$  and 5  $\mu\text{m}$  at high throughput is also possible, thereby paving the way for interesting biological applications, where a high-pass filter with a higher Q-value (i.e. narrower separation band of 2/5  $\mu\text{m}$  vs. 3/10  $\mu\text{m}$ ) is desirable.

### 3.6 Frequency modulation.

When optimizing the device in the course of the separation experiments, we saw some effects from geometry-induced acoustic streaming especially at the glass divider (a critical place). From the theoretical arguments, we know that at a resonant frequency with a pressure half-wave in the height dimension, there will be other frequencies close by in frequency space, with similar pressure half-waves in the height dimension, only differing by the number of half-waves along the width and length of the device, see Fig. 3.6. As it turns out, there is no such systematization in the acoustic streaming phenomena, and the acoustic streaming patterns for two frequencies are completely different, even if the two frequencies are very close in frequency space.

In a paper by Manneberg *et al.* in *Lab-on-a-Chip*, 2009[18] it was demonstrated, that by sweeping the piezo actuation frequency linearly around the resonant frequency with a modulation period on the order of microseconds, it was possible to average out the forces from several slightly imperfect fixed-frequency modes to get one stable average-mode. We found, that sweeping linearly  $\pm \sim 10$  kHz around the resonant frequency, the separation efficiency was increased. Furthermore, it was observed in the microscope, that the

---

<sup>5</sup>we will be building a final third-generation device before we spend time collecting publication-data in triplicates, more on this in Chapter 4

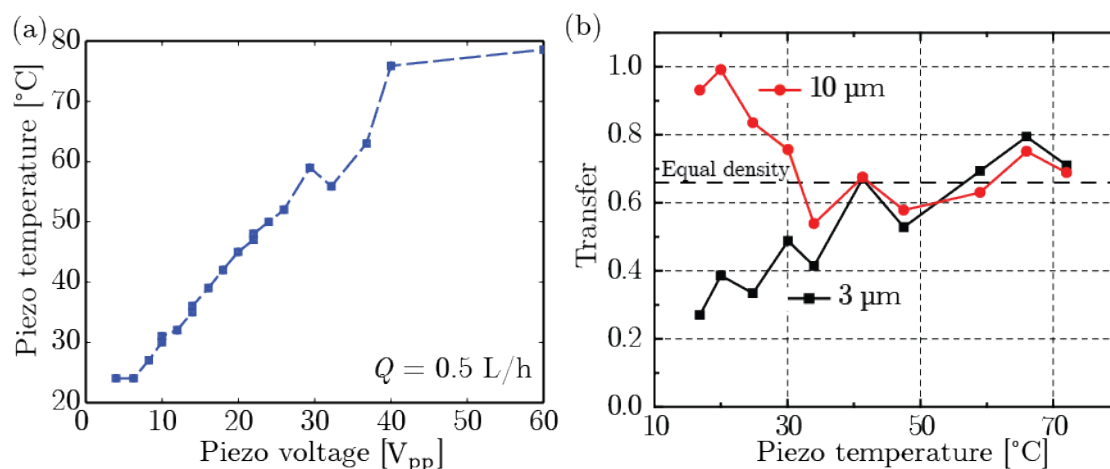


Figure 3.14: Experimentally observed temperature effects. (a) Piezo self-heating as a function of piezo voltage at 0.5 L/h throughput. The temperature in this particular series was measured with a chromel/alumel mounted on the side of the device giving an approximate uncertainty of 0.5°C, errorbars plotted. The voltage was measured peak-to-peak with a digital oscilloscope giving a neglectable uncertainty. (b) Separation degradation due to heating, demonstrating the importance of temperature control. The speed of sound in water changes  $\approx 10\%$  between 0°C and 100°C, so heating will shift the device off resonance. Above 35°C, we see a transfer of  $\approx 0.66$ , corresponding to equal density in both outlets (total mixing).

effects from acoustic streaming were dramatically reduced. Sweeping in larger or smaller frequency windows or with longer modulation periods seemed to not work as well (data not shown). From a fabrication point of view, there is a very nice side-point to the frequency modulation; When constructing the device, it is highly possible, that the device symmetry gets broken by slight misalignment of the device layers. We believe that sweeping the frequency can in general help overcome the effects of these manufacture imperfections.

An improvement over the frequency-modulation technique presented by Manneberg *et al.* would be to rapidly switch back and forth between different *resonant* modes, all with a half-wave in the height dimension, but with different numbers of axial half-waves, instead of just sweeping around a resonant frequency. The different resonances should have radically different streaming patterns, but all have a strong pressure resonance for acoustic separation, thus eliminating the streaming effects while maintaining a strong force field for acoustophoretic separation. This is not something that has been reported in the literature before. We have not been able to fully implement and test this feature before the deadline of this thesis, but it should be possible to find several working frequencies and program the digital function generator to switch rapidly between them to increase the separation efficiency.

### 3.7 Temperature effects

Another very important feature of our device setup is the temperature control. Studies of the temperature effects in acoustophoresis has not been reported in the literature before, but we report that in our large device, temperature control is a necessary prerequisite for achieving the high-throughput separation reported in Fig. 3.13. Using the Peltier element and the thermocouple mounted as in Fig. 3.1(b), we are able to keep the device at a constant temperature during the course of a separation experiment. This is very important in biological applications where it is necessary to handle cells at constant temperature, e.g. for incubation 5 °C or 37 °C and is necessary to ensure stability of the pressure resonance making it an important prerequisite for achieving the high-throughput separation. If the device is not temperature controlled, substantial piezo self-heating is seen, as shown in Fig. 3.14(a). The piezo voltage was measured peak-to-peak with a digital oscilloscope and the device temperature was measured with a chromel/alumen thermocouple set in thermal grease on the side of the device. The piezo self-heating is due to a slight delay in piezo-polarization response to the applied electric field during an oscillation period and the approximately linear relation between applied piezo voltage and piezo temperature is consistent with the literature[31, 30].

In Fig. 3.14(b), we show another key result of this thesis; The increase of device temperature leads to separation efficiency degradation, demonstrating the importance of temperature control. The speeds of sound in water and glass changes with temperature (approximately 10% between 0°C and 100°C in the case of water[4]), so heating will shift the device off resonance. The physical properties of the piezo actuator will also change with temperature, changing the piezoelectric response amplitude and thereby affecting the resonances. Above 35°C, we see a transfer of  $\approx 0.66$ , corresponding to equal bead density in both outlets (i.e. total mixing by non-resonant acoustic waves). From Fig. 3.9, we know that at 1 L/h flowrate the characteristic velocity in the separation channel is on the order of cm/s. Using the channel height as the characteristic length-scale, this gives a thermal Peclet-number for the flow,  $Pe_{th} = V_0 L_0 / D_{th} \approx 57$ . Given our very long microchannel, we expect that this actually allows for the build-up of temperature gradients across the channel. This was verified by calculating the temperature field in the device using a finite element method in COMSOL, see Fig. 3.15. We investigated a 2D model of the device, as the large aspect ratio of the microchannel made it impossible to mesh and solve a full 3D model. We solved the heat equation, Eq. (2.17), which in steady-state with no heat sources/sinks and disregarding viscosity becomes,

$$\rho c_p v_j \partial_j T = \kappa \partial_j^2 T \quad (3.18)$$

It can be shown by perturbation expansion calculations, that even though viscosity,  $\eta(T)$ , density,  $\rho(T)$ , and thermal conductivity,  $\kappa(T)$ , depend slightly temperature, to a very good approximation, the velocity profile responsible for convective heat transfer in the channel is simply the usual parabolic Poiseuille flow profile[5], Eq. (2.9), which in the 2D model reduces to flow between two infinite parallel plates,

$$v_x(z) = \frac{6Q_{total}}{h_0 w_0} (h_0 - z)z, \quad (3.19)$$

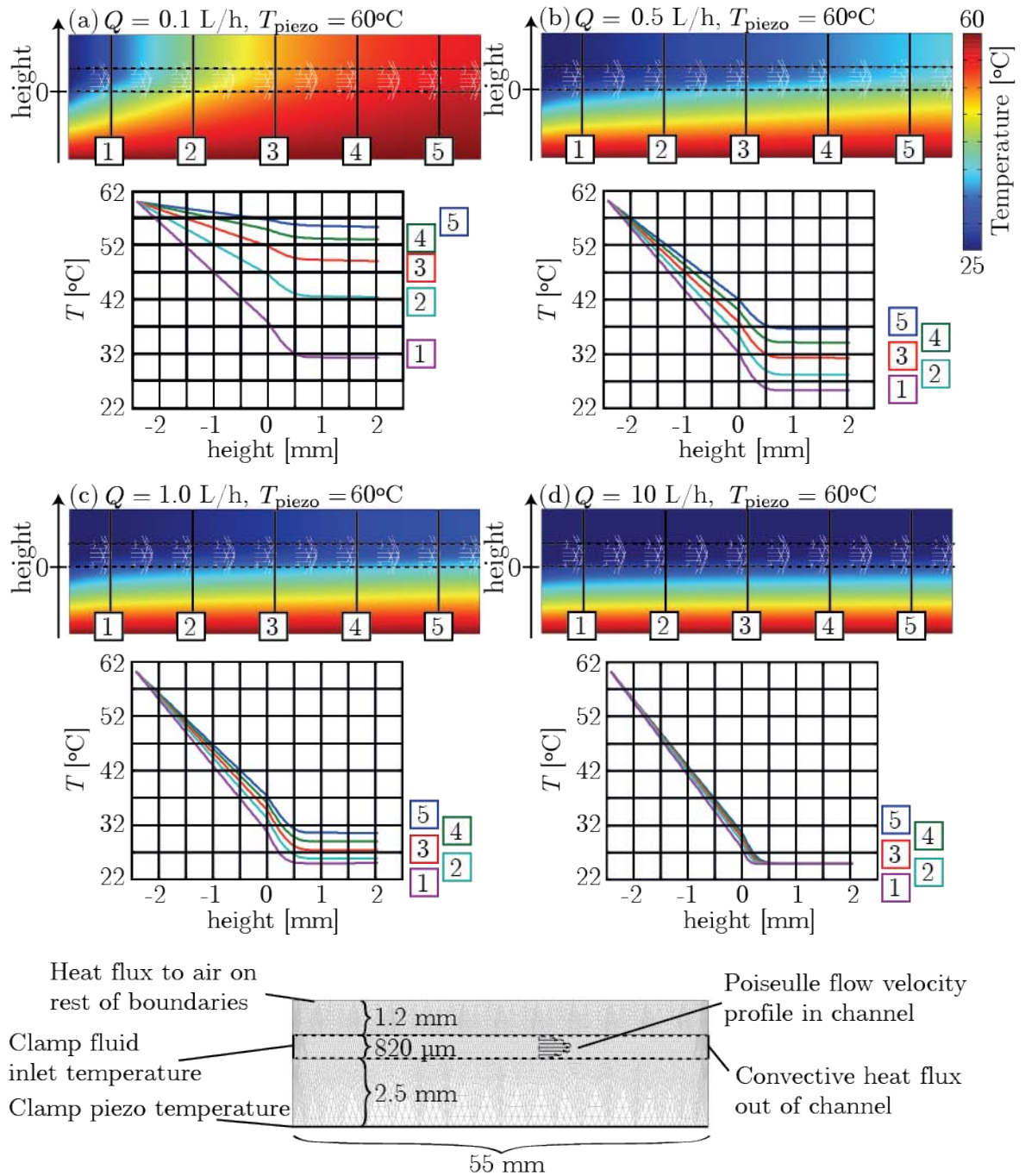


Figure 3.15: Finite element method calculation of device temperature field. (Bottom) Sketch of the simplified 2D finite element model solved in COMSOL and checked with convergence analysis to be sufficiently meshed. Not drawn to scale. We neglect effects from the 100  $\mu\text{m}$  epoxy layer in the thick glass divider and model a 55 mm  $\times$  (2.5, 0.82, 1.2) mm glass/water/glass-sandwich device. (a)-(d) Color plots of the temperature field in the device bound to a 60°C piezo at increasing flowrates. The dashed black lines mark the water channel and the white arrows show the direction and relative magnitude of the Poiseuille flow velocity profile in arbitrary units. Line plots show the temperature profile across the device height at five points along the device length.

Table 3.1: Thermal properties of water and pyrex glass[17].

	$\rho$ kg/m <sup>3</sup>	$c_p$ J/(kg K)	$\kappa$ W/(K m)
water	998	4180	1.0
pyrex glass	2230	840	0.6

where  $w_0$  and  $h_0$  are the width and height of the actual channel, respectively, and  $Q_{\text{total}}$  is the total flowrate. The boundary conditions were as follows (confer Fig. 3.15): (i) At the piezo (bottom) we clamp the temperature with a Dirichlet condition, so  $T = T_{\text{piezo}}$ . (ii) At the channel inlet (left), we also clamp the temperature with a Dirichlet condition, so  $T = T_{\text{room}}$ . (iii) At the channel outlet (right), we allow heat flux due to convection with a Neumann condition,  $\mathbf{n} \cdot (\kappa \nabla T) = \mathbf{n} \cdot (\rho c_p T \mathbf{v})$ . (iv) At the water/glass interfaces we require continuity of flux and temperature with a Cauchy condition,  $\mathbf{n} \cdot (\kappa_{\text{py}} \nabla T_{\text{py}} - \kappa_{\text{wa}} \nabla T_{\text{wa}})$  and  $T_{\text{py}} = T_{\text{wa}}$ . (v) At all other boundaries, we model heat flux to the surrounding air with a Neumann condition,  $\mathbf{n} \cdot (\kappa \nabla T) = K_{\text{air}}(T - T_{\text{room}})$ , where  $K_{\text{air}} \approx 7.5 \text{ W/Km}^2$  is a material parameter. Other thermal parameters for water and pyrex glass are shown in Table 3.1.

Fig. 3.15 shows the temperature field in a second-generation device bound to a 60 °C piezo at different flowrates, with inserted lineplots showing the temperature across the channel height at different positions down the device length, obtained by a finite element method in COMSOL. We see that for low flowrates, the whole device becomes heated, so the temperature becomes almost uniform across the whole device height, see Fig. 3.15(a). For larger flowrates, the device is so to speak *self-cooled* by the sample flow so the channel temperature is at least almost uniform across the channel length, see Fig. 3.15(b)-Fig. 3.15(d). However, for the 1 L/h total flowrate we have used, we still see a large temperature gradient across the bottom glass reflectors and a gradient of  $\sim 6 \text{ }^\circ\text{C}$  across the water channel (height = 0  $\mu\text{m}$  - 820  $\mu\text{m}$ ), see Fig. 3.15(c). We believe the main effect of these temperature variations across the device are on the speeds of sound in glass and pyrex. Even for fixed frequencies at temperatures above room temperature, the separation efficiency of the device was seen to be diminished (data not shown). We believe that the nonuniformity of the temperature fields can explain this effect; The nonuniform temperature fields break the symmetry in the device geometry affecting the stability and symmetry of the resonant modes. This is something, that has not been discussed in the literature before. Further theoretical insight into the exact effect on the resonances could be reached by coupling the temperature fields to the acoustic fields through the variations in speed of sound, but this lies beyond the scope of this particular thesis.

## Chapter 4

# Conclusion and future work

In this thesis we have presented the design of a microfluidic chip capable of acoustophoretic separation and shown experimental separation of 3  $\mu\text{m}$  and 10  $\mu\text{m}$  polystyrene microparticles at the very high throughput of 1 L/h. This throughput is approximately hundred times higher than previously reported in the literature [14, 16]. Our device is constructed from low-cost materials readily available in most labs without the use of time-consuming clean room techniques making our design cheap and easy to copy and employ elsewhere. We find evidence that by frequency sweeping of the piezo actuation frequency in the acoustophoretic separation, the microparticle bands becomes more stable and tightly focussed leading us to believe, that the sweeping is a clever way to overcome effects on the acoustic resonances from slight device geometry symmetry breaking induced in the non-cleanroom fabrication.

This thesis also provides a very good example of how a comprehensive theoretical understanding and analysis of the device physics in close conjunction with experimental test is needed to *actually* make such a device work. We thoroughly review the acoustic, fluidic and thermal properties of our device both experimentally and theoretically to be able to optimize the device and make it fully functional. This comprehensive analysis of the device is not something that is very common in the acoustophoresis-literature, and from our theoretical analysis, we are able to introduce two very important new concepts. Firstly, we show that by matching the device geometry to the acoustic wavelengths in the various device materials (e.g. channel with matched to glass reflector thickness, asymmetric glass reflectors), the device can be optimized for stronger acoustic fields and better acoustophoretic separation. Secondly, we show that good temperature control is a prerequisite for our large device to function. We hypothesize that because large temperature gradients across the device change the speed of sound in the device materials, heating will shift the device of resonance and break the device symmetry, and we see experimentally that heating does indeed reduce the separation to complete mixing of microparticle species.

Furthermore, we have show that as a novelty for our very low-fluidic-resistance device with the large high-throughput channel, a thorough analysis of the device and external fluidics is necessary to ensure the desired flow in the device and we show, that as a novelty

for our device, the internal flow pattern can be easily modified by changing the resistance of the external fluidics. All these small, but crucial, details must be considered and controlled for our device to work, and this is where a good theoretical analysis combined with experiments really shows its strength.

We intend to submit the work presented in this thesis as a paper to a journal in the scientific literature, but before this is done, we intend to add two more points to the story. Firstly we see in Fig. 3.13(c), that the device separated the 3  $\mu\text{m}$  and 10  $\mu\text{m}$  microparticles at a piezo voltage of  $\sim 15 V_{\text{pp}}$ . We showed in Section 3.1, that the scoustophoretic force scales with the piezo voltage squared,  $F_{\text{ac}} \propto V^2$ . Our current electric setup allows us to run the piezo at  $\sim 60 V_{\text{pp}}$  with no appreciable signal distortion and with out temperature controlled setup, we are able to maintain a constant temperature. By increasing the voltage 4-fold from  $\approx 15 V_{\text{pp}}$  to  $60 V_{\text{pp}}$ , we should get a 16-fold stronger force field and thusly be able to run the device much faster. Our current flowrate is limited by the max flowrate of the syringe pumps available to us, but we have designed and are amidst constructing a custom-built pressure driven pumping system capable of much higher flowrates. We hope to be able to show successful separation at  $\approx 10 \text{ L/h}$ , a 1000-fold improvement over the state of the art. Secondly, we intend to show the usefulness of the device in biological and medical applications by demonstrating separation of some relevant cells. We have shown preliminary results for separation of 2  $\mu\text{m}$  and 5  $\mu\text{m}$  polystyrene microparticles, which we expect to improve by optimization, and we believe, that separation of cells of the same sizes will be possible.

Whole blood contains platelets (2 – 3  $\mu\text{m}$ ), red blood cells (6 – 8  $\mu\text{m}$ ) and white blood cells (7 – 8  $\mu\text{m}$  for lymphocytes,  $> 10 \mu\text{m}$  for all others)[2]. We hope to show the application of the device for (i) Separation of red and white blood cells from an undiluted whole blood sample, yielding blood plasma. This would be a very nice medical application, where the throughput can rival current state-of-the-art methods like centrifugation. In usual plasmapheresis, 550 mL of plasma is donated in about 45 minutes, a time we would be able to improve significantly. We do not expect the shear rates of the device to be high enough for platelet activation in the device. (ii) Separation of white blood cells from an undiluted whole blood sample. This would also be a very nice medical application, where the high-throughput is a key element. Separation of white blood cells is currently done with centrifugation methods and pharmacological tools and since only about one in every thousand blood cell is a white blood cell, it is necessary to analyze a quite large blood sample in order to collect enough white blood cells for e.g. some diagnostics. The high-throughput device would be able to collect the white blood cells from a large sample very fast, with high purity and without introducing pharmacological tools that may chemically affect the cells and influence a diagnostics read-out.

A minor thing that might be worthwhile to do as well, would be to use the temperature controlled setup to show cell separation at different biologically relevant constant temperatures (e.g. 5  $^{\circ}\text{C}$  or 37  $^{\circ}\text{C}$ ). This is also something, that has not been reported in the literature before.

All these things will be done on a third-generation device, we will build. The only change from the second-generation device to the third-generation device will be nicer materials to ensure better device symmetry and even easier and faster fabrication; the

thin glass divider will be made from a smooth, industrially machined 50  $\mu\text{m}$ -wafer, the thick glass reflector will be made from one thick glass piece instead of two epoxy-bonded microscope slides and the device will be actuated by one large rectangular piezo actuator underneath the channel instead of two square piezo actuators side by side.



## Appendix A

# Abstract for micro-TAS 2010

Reprinted on the following two pages is an abstract submitted for The 14th International Conference on Miniaturized Systems for Chemistry and Life Sciences (micro-TAS or  $\mu$ TAS), to be held 3 - 7 October 2010 in Groningen, The Netherlands, during the work on this thesis. The abstract was submitted for oral presentation in the *Cell Handling and Sorting* subconference.

Topic No. 1.6: Cell Handling and Sorting  
Oral presentation preferred

Paper ID No: 0935

**Temperature-controlled high-throughput (1 L/h) acoustophoretic particle separation in microchannels**

C. L. Ebbesen<sup>(a)</sup>, J. D. Adams<sup>(b)</sup>, R. Barnkob<sup>(a)</sup>, H. T. Soh<sup>(c)</sup>, and H. Bruus<sup>(a)</sup>

<sup>(a)</sup>Department of Micro- and Nanotechnology, Technical University of Denmark, DENMARK

<sup>(b)</sup>Physics Department, University of California, Santa Barbara, USA

<sup>(c)</sup>Mechanical Engineering and Materials Departments, University of California, Santa Barbara, USA

Separation and purification of target particles/cells from complex mixtures is a critical step in many diagnostic and therapeutic applications. Toward this end, there has been significant interest in microchannel acoustophoresis because it allows gentle, label-free separation based on size, density and compressibility [1–6]. Unfortunately, hitherto, the low throughput of microfluidic systems ( $\lesssim 0.03$  L/h [1]), has limited its broader use in biotechnology. Here, we present a microfluidic acoustophoretic separator capable of unprecedented high throughput (above 1 L/h), approximately hundred times higher than previously reported [1, 5]. It is fabricated by low-cost rapid-prototyping techniques, facilitating easy and versatile application.

Our device consists of one broad microchannel ( $60 \text{ mm} \times 17 \text{ mm} \times 830 \text{ }\mu\text{m}$ ) equipped with two inlet/outlet pairs and fabricated from PDMS gaskets, cut from  $250 \text{ }\mu\text{m}$  PDMS sheets using a plotting cutter, plasma bonded between standard microscope slides (Fig. 1). The slides, bonded together using epoxy glue, act as acoustic reflectors. The central flow-divider, milled using a CNC-drill from a thin glass slide, is  $70 \text{ }\mu\text{m}$  thick. Two  $27 \text{ mm} \times 27 \text{ mm}$  piezoelectric transducers, attached beneath (using super glue) and fully covering the separation channel, induce a strong acoustic resonance in the microchannel when powered by a sinusoidal voltage at  $899 \text{ kHz}$  and  $1 - 30 \text{ V}_{pp}$ .

To characterize the purity and throughput of the device, we prepared a sample mixture of red fluorescent  $3\text{-}\mu\text{m}$ -diameter and green fluorescent  $10\text{-}\mu\text{m}$ -diameter polystyrene beads (mimicking typical cell sizes) suspended in a DI water buffer with  $0.01 \text{ v/v } \%$  tween-20. The sample and buffer are injected by syringe pumps into the device at flow rates of  $0.25$  and  $0.75 \text{ L/h}$ , respectively. Outlet samples are collected in microcentrifuge tubes during separation, and the bead density is determined by flow cytometry.

Figure 2(a) shows successful separation of  $3\text{-}\mu\text{m}$  and  $10\text{-}\mu\text{m}$  microbeads at the high  $1 \text{ L/h}$  flow rate. The mutual orthogonality of the flow direction (length), the throughput dimension (width), and the force direction (height) is the main prerequisite for our result. However, to ensure stability of the acoustic resonance, we employed two additional features: (1) As a novelty in microchannel acoustophoresis, Fig. 2(b) shows that the separation efficiency at a given frequency is highly temperature dependent. Our high flow rate requires a strong force field (high piezo voltage) leading to heating, which shifts the resonance frequency. Temperature stability ( $< \pm 1 \text{ }^\circ\text{C}$ ) is maintained using a Peltier-element attached beneath the piezos. (2) To reduce separation degradation from acoustic streaming near the flow divider [7], we apply a  $1 \text{ ms}$  linear frequency sweep [3] in a  $20\text{-kHz}$ -window around the center frequency.

Using our orthogonal-direction device geometry we have demonstrated very high throughput ( $1 \text{ L/h}$ ) acoustophoretic separation. The present throughput is limited by syringe pump capacities, not by separation forces; our temperature control allows a 4-fold actuation voltage increase without heating, leading to a 16-fold increase in the acoustic force-field. Ongoing work includes development of faster feeding pumps and applications in biological cell separation.

Word count: 496 (<http://www.globalrendering.com/download.html>)

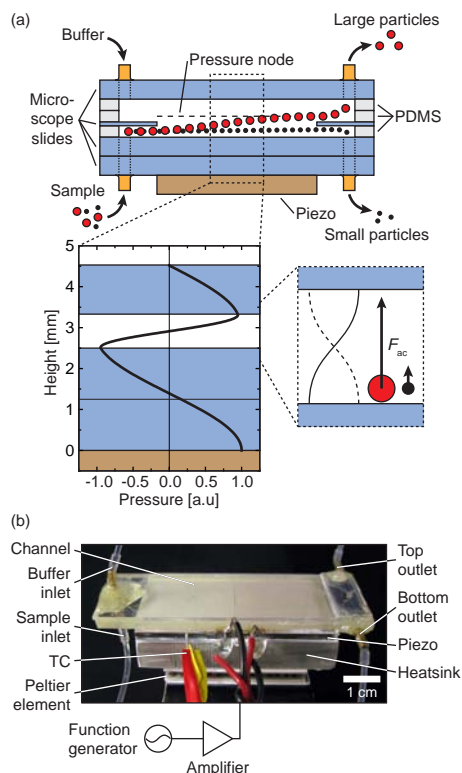


Figure 1: (a) Design schematic of the high-throughput device showing pressure resonance (black line) and acoustic radiation force (black arrows). The geometry of the device is designed to support a standing half-wave in the pressure field across the height of the microchannel. (b) The device is mounted in a stable fluidic setup with 500  $\mu\text{m}$ -diameter teflon tubing. The hydraulic resistance (length) of the outlet tubing is matched to ensure a correct outlet flow ratio. The temperature of the device is measured using a chromel/alumel thermocouple (TC). The device is mounted in thermal compound on an aluminum heat sink and cooled by a Peltier element.

#### References

- [1] T. Laurell, F. Petersson, and A. Nilsson, *Chem. Soc. Rev.* **36**, 492 (2007).
- [2] F. Petersson, L. Åberg, A.-M. Sward-Nilsson and T. Laurell, *Anal. Chem.* **79**, 5117 (2007).
- [3] O. Manneberg, B. Vanherberghen, B. Onfelt, and M. Wiklund, *Lab Chip* **9**, 833 (2009).
- [4] T. Franke, S. Braummüller, L. Schmid, A. Wixforth, and D. A. Weitz, *Lab Chip* **10**, 789 (2010).
- [5] A. Lenshof and T. Laurell, *Chem. Soc. Rev.* **39**, 1203 (2010).
- [6] P. Thévoz, J. D. Adams, H. Shea, H. Bruus, H. T. Soh, *Anal. Chem.* **82**, 3094 (2010).
- [7] S. M. Hagsäter *et al.*, *Lab Chip* **8**, 1178 (2008).

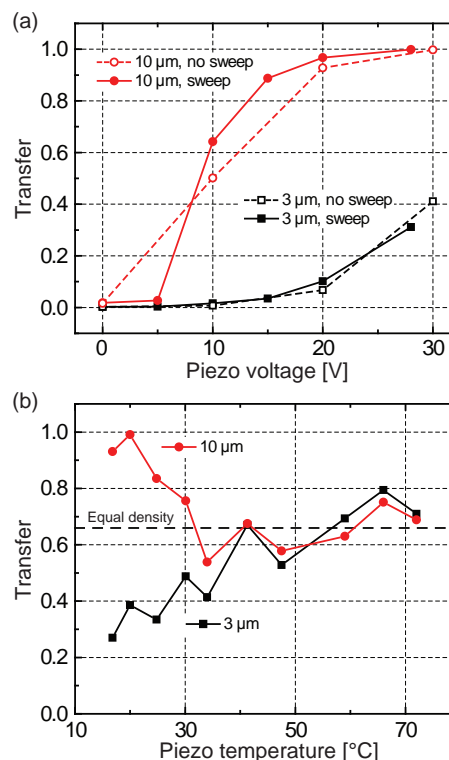


Figure 2: (a) Fraction of beads in the top outlet (transfer) at 1 L/h throughput showing strong separation at 15  $V_{pp}$  and  $f_{center} = 899$  kHz. Sweeping around  $f_{center}$  increases separation efficiency. The data have been corrected for a small background, measured by running the device with buffer in both inlets. (b) Separation degradation due to heating, demonstrating the importance of temperature control. The speed of sound in water changes  $\approx 10\%$  between  $0^\circ\text{C}$  and  $100^\circ\text{C}$ , so heating will shift the device off resonance. Above  $35^\circ\text{C}$ , we see a transfer of  $\approx 0.66$ , corresponding to equal density in both outlets (total mixing).



# Bibliography

- [1] Jonathan D Adams, Patrick Thévoz, Henrik Bruus, and H Tom Soh. Integrated acoustic and magnetic separation in microfluidic channels. *Applied physics letters*, 95(25):254103, December 2009.
- [2] B. Alberts, A. Johnson, J. Lewis, M. Raff, K. Roberts, and P. Walter. *Molecular biology of the cell*. Garland Science, New York, 5th edition, 2007.
- [3] Rune Barnkob, Per Augustsson, Thomas Laurell, and Henrik Bruus. Measuring the local pressure amplitude in microchannel acoustophoresis. *Lab on a chip*, 10(5):563–70, March 2010.
- [4] Nikolai Bilaniuk. Speed of sound in pure water as a function of temperature. *The Journal of the Acoustical Society of America*, 93(4):2306, 1993.
- [5] Henrik Bruus. *Theoretical Microfluidics*. Oxford University Press, 2nd edition, 2008.
- [6] Henrik Bruus. *Microfluidics and ultrasound acoustophoresis*. Number June. Lecture notes for the advanced CISM school, Udine, Italy, 7 - 11 June 2010: Ultrasound standing wave action on suspensions and biosuspensions in micro- and macrofluidic devices., 1st edition, 2010.
- [7] L. P. Gorkov. On the forces acting on a small particle in an acoustic field in an ideal fluid. *Sov. Phys. Doklady*, 6:773–776, 1962.
- [8] Daniel R Gossett, Westbrook M Weaver, Albert J Mach, Soojung Claire Hur, Henry Tat Kwong Tse, Wonhee Lee, Hamed Amini, and Dino Di Carlo. Label-free cell separation and sorting in microfluidic systems. *Analytical and bioanalytical chemistry*, April 2010.
- [9] C. Grenvall, P. Augustsson, J. Folkenberg, and T. Laurell. Harmonic Microchip Acoustophoresis: A Route to Online Raw Milk Sample Precondition in Protein and Lipid Content Quality Control. *Analytical Chemistry*, 81(15):6195–6200, 2009.
- [10] S. M. Hagsäter, A. Lenshof, P. Skafte-Pedersen, J. P. Kutter, T. Laurell, and H. Bruus. Acoustic resonances in straight micro channels: Beyond the 1D-approximation. *Lab on a Chip*, 8(7):1178, 2008.

- [11] Jeremy J. Hawkes, Robert W. Barber, David R. Emerson, and W. Terence Coakley. Continuous cell washing and mixing driven by an ultrasound standing wave within a microfluidic channel. *Lab on a Chip*, 4(5):446, 2004.
- [12] L. D. Landau and E. M. Lifshitz. *Statistical Physics (Course of Theoretical Physics, Volume 5)*. Butterworth-Heinemann, 3rd edition, 1980.
- [13] L. D. Landau and E. M. Lifshitz. *Fluid Mechanics (Course of Theoretical Physics, Volume 6)*. Butterworth-Heinemann, 2nd edition, 1987.
- [14] Thomas Laurell, Filip Petersson, and Andreas Nilsson. Chip integrated strategies for acoustic separation and manipulation of cells and particles. *Chemical Society Reviews*, 36(3):492, 2007.
- [15] Andreas Lenshof, Asilah Ahmad-Tajudin, Kerstin Järås, Ann-Margret Swärd-Nilsson, Lena Aberg, György Marko-Varga, Johan Malm, Hans Lilja, and Thomas Laurell. Acoustic whole blood plasmapheresis chip for prostate specific antigen microarray diagnostics. *Analytical chemistry*, 81(15):6030–7, August 2009.
- [16] Andreas Lenshof and Thomas Laurell. Continuous separation of cells and particles in microfluidic systems. *Chemical Society Reviews*, 39(3):1203–17, March 2010.
- [17] David R. Lide, editor. *Handbook of Chemistry and Physics*. CRC Press, Boca-Raton, 84th edition, 2003.
- [18] O Manneberg, B Vanherberghen, B Onfelt, and M Wiklund. Flow-free transport of cells in microchannels by frequency-modulated ultrasound. *Lab on a chip*, 9(6):833–7, March 2009.
- [19] J. Nilsson, M. Evander, B. Hammarström, and T. Laurell. Review of cell and particle trapping in microfluidic systems. *Analytica chimica acta*, 649(2):141–57, September 2009.
- [20] Jessica Voorhees Norris, Mikael Evander, Katie M Horsman-Hall, Johan Nilsson, Thomas Laurell, and James P Landers. Acoustic differential extraction for forensic analysis of sexual assault evidence. *Analytical chemistry*, 81(15):6089–95, August 2009.
- [21] J.R. O’Brien and G.P. Salmon. Shear Stress Activation of Platelet Glycoprotein IIb/IIIa Plus von Willebrand Factor Causes Aggregation: Filter Blockage and the Long Bleeding Time in Von Willebrand’s Disease. *Blood*, 70(5):1354–1361, 1987.
- [22] Filip Petersson, Lena Aberg, Ann-Margret Swärd-Nilsson, and Thomas Laurell. Free flow acoustophoresis: microfluidic-based mode of particle and cell separation. *Analytical chemistry*, 79(14):5117–23, July 2007.
- [23] Filip Petersson, Andreas Nilsson, Cecilia Holm, Henrik Jonsson, and Thomas Laurell. Separation of lipids from blood utilizing ultrasonic standing waves in microfluidic channels. *The Analyst*, 129(10):938–43, October 2004.

- [24] J. Pfitzner. Poiseuille and his law. *Anaesthesia*, 1(1):273–275, March 1976.
- [25] Moitreyee Sinha and Donald J Buckley. *Acoustic Properties of Polymers*, volume 1, chapter 60, pages 1021–1031. Springer, New York, 2nd edition, 2007.
- [26] Peder Skafte-Pedersen. *Acoustic forces on particles and liquids in microfluidic systems*. Master thesis, DTU Nanotech, 2008.
- [27] Patrick Thévoz, Jonathan D Adams, Herbert Shea, Henrik Bruus, and H Tom Soh. Acoustophoretic synchronization of mammalian cells in microchannels. *Analytical chemistry*, 82(7):3094–8, April 2010.
- [28] Jean K Tsou, Jie Liu, Abdul I Barakat, and Michael F Insana. Role of ultrasonic shear rate estimation errors in assessing inflammatory response and vascular risk. *Ultrasound in medicine & biology*, 34(6):963–72, June 2008.
- [29] Søren 'BS Chuck' Vedel. Investigation of Taylor-Aris dispersion in heat transport, 2010.
- [30] Zhengbin Wu and Sandy Cochran. Loss effects on adhesively-bonded multilayer ultrasonic transducers by self-heating. *Ultrasonics*, 50(4-5):508–11, April 2010.
- [31] J. Zheng, S. Takahashi, S. Yoshikawa, and K. Uchino. Heat Generation in Multilayer Piezoelectric Actuators. *J. Am. Ceram. Soc.*, 79(12):3193–3198, 1996.